NOVA SCHOOL OF SCIENCE & TECHNOLOGY

MATERIALS SCIENCE DEPARTMENT

DUARTE CORREIA DA FONSECA DA SILVA ANTUNES

BSc in Micro & Nano Technologies

SOLAR FUELS DESIGN: MODELING POROUS CATHODES FOR THE PRODUCTION OF CARBON-BASED FUELS FROM CO_2

COMSOL MULTIPHYSICS® MODELING APPROACH

MASTER IN MICRO & NANO TECNHOLOGIES

NOVA University Lisbon

October, 2022

NOVA SCHOOL OF SCIENCE & TECHNOLOGY

MATERIALS SCIENCE DEPARTMENT

SOLAR FUELS DESIGN: MODELING POROUS CATHODES FOR THE PRODUCTION OF CARBON-BASED FUELS FROM CO_2

COMSOL MULTIPHYSICS® MODELING APPROACH

DUARTE CORREIA DA FONSECA DA SILVA ANTUNES

BSc in Micro & Nano Technologies

Adviser: Dr. Manuel João de Moura Dias Mendes
Auxiliary Professor, NOVA University Lisbon

Co-adviser: Dr. Ana Maria Staack Reis Machado
Researcher, NOVA University Lisbon

Examination Committee:

Chair: Dr. Rodrigo Ferrão de Paiva Martins,
Full Professor, FCT NOVA

Rapporteurs: Dr. Carmen Mireya Rangel Archila,
Coordinating Researcher, LNEG

Adviser: Dr. Manuel João de Moura Dias Mendes,
Auxiliary Professor, FCT NOVA

Members: Dr. Ana Maria Staack Reis Machado,
Researcher, FCT NOVA

MASTER IN MICRO & NANO TECHNOLOGIES

NOVA University Lisbon
October, 2022

Solar Fuels Design: Modeling Porous Cathodes for the Production of Carbon-Based Fuels from CO_2

Acknowledgments

Antes de mais, gostaria de agradecer ao Professor João Paulo Borges, Presidente do Departamento de Ciência dos Materiais (DCM). Agradecer também ao Professor Hugo Manuel Águas, Coordenador do Curso onde me insiro, Mestrado Integrado em Engenharia de Micro e Nanotecnologias (MIEMN). Gostaria também de agradecer ao Dr. Rodrigo Martins e à Dra. Elvira Fortunato, por criarem este curso único, a que me dediquei nestes últimos cinco anos.

Quero também fazer um agradecimento especial ao Professor Manuel João Mendes, meu Orientador, e à Dr.ª Ana Reis Machado, minha Coorientadora, pela oportunidade de trabalhar neste tema inovador que se enquadra com os meus interesses e motivações futuras e da mesma forma à Inês Fernandes, pela ajuda prestada sempre que a solicitei.

Um agradecimento a todos os professores que me acompanharam durante estes 5 anos, que me ajudaram a crescer e a amadurecer como pessoa e futuro engenheiro.

Da mesma forma, não posso deixar de agradecer aos colegas que me acompanharam durante esta trajetória, com quem trabalhei e estudei e travei amizade, em especial ao Dinis, Tomás e Diogo.

O maior dos agradecimentos à minha mãe e padrasto, por tudo o que me proporcionaram e por apoio incondicional ao longo dos meus 22 anos, aconselhando, abrindo horizontes, fazendo-me refletir, mas dando espaço às minhas escolhas e opções.

Não posso esquecer também da minha namorada, Juliana Domingues, pela sua presença, força e motivação nestes últimos anos para poder superar e conseguir alcançar todos os meus objetivos.

Finalmente, queria agradecer à Fundação para a Ciência e a Tecnologia por ter financiado os Projetos CO_2RED, com a referência PTDC/EQU-EPQ/2195/2021, e CO_2Value (MIT-EXPL/CS/0052/2021), que possibilitaram a realização deste trabalho.

Abstract

The use of fossil fuels is related to several environmental hazards, including global warming, which is caused by an excess of CO_2 in the atmosphere. The reduction of CO_2 emissions from industrial waste gases is crucial for reducing the atmospheric greenhouse effect and, hence, combating climate change. There are several technologies for CO_2 utilisation, powered by electricity derived from solar energy, which can be used to transform fundamental chemical feedstocks like CO_2 and water into clean alternative fuels that improve grid stability, energy security, and environmental advantages. Furthermore, Electrochemical CO_2 Reduction (CO_2R) is one of the most promising strategies to achieve this goal.

A two-dimensional model for porous electrodes developed by C. Ma *et al*. (2018) to design electrodes for a flow-through, quinone-based battery was adapted in this Thesis to allow the design and optimization of a porous zinc cathode for an electrolizer to perform the co-electrolysis of CO_2 and water. COMSOL® software was used to run the simulations, while model validation was conducted using the experimental data provided by Luo *et al.* (2019).

The impacts of porosity, pore length, fiber shape geometry, pressure and temperature were explored, and after analyzing the performance of the electrode in each condition, it was possible to optimize each of the previously mentioned parameters and achieve considerably higher current density values (up to 190.06 mA/cm^2) than those reported in the literature.

Keywords: Environmental hazards, Renewable Fuels, Electrochemical CO_2 Reduction, COMSOL® software, Porous Electrodes.

Resumo

A utilização de combustíveis fósseis está relacionada com vários perigos ambientais, incluindo o aquecimento global, que é causado por um excesso de CO_2 na atmosfera. A redução das emissões de CO_2 dos gases de resíduos industriais é crucial para reduzir o efeito de estufa atmosférico e, consequentemente, para combater as alterações climáticas. Existem várias tecnologias para a utilização de $CO2$, alimentadas por eletricidade obtida a partir da energia solar, que podem ser utilizadas para transformar matérias-primas químicas fundamentais como o $CO2$ e a água em combustíveis alternativos limpos que melhoram a estabilidade da rede, a segurança energética, e as vantagens ambientais. Além disso, a Redução Eletroquímica do CO_2 (CO_2R) é uma das estratégias mais promissoras para atingir este objectivo.

Um modelo bidimensional para elétrodos porosos desenvolvido por C. Ma *et al.* (2018) para a conceção de elétrodos para uma bateria à base de quinona foi adaptado nesta Tese para permitir a conceção e otimização de um cátodo de zinco poroso para um eletrolisador a fim de realizar a co-electrólise de CO_2 e água. O software COMSOL® foi utilizado para executar as simulações, enquanto a validação do modelo foi realizada utilizando os dados experimentais fornecidos por Luo *et al.* (2019).

Foram explorados os impactos da porosidade, comprimento dos poros, geometria da forma da fibra, pressão e temperatura, e após análise do desempenho do elétrodo em cada condição, foi possível otimizar cada um dos parâmetros anteriormente mencionados e alcançar valores de densidade de corrente consideravelmente mais elevados (até 190.06 mA/cm^2) do que os reportados na literatura.

Palavras-chave: Perigos ambientais, Combustíveis renováveis, Redução Eletroquímica de CO_2, Software COMSOL®, Elétrodos porosos.

Contents

1 INTRODUCTION 1

2 MATERIALS AND METHODS 7

3 RESULTS AND DISCUSSION 9

3.1 Model Description and Geometry 9

3.1.1 Model Purposes 10

3.1.2 Mathematical Model Development 11

3.1.2.1 Fluid Flow Model 11

3.1.2.2 Mass Transport and Electrochemical Model 11

3.1.3 Model Boundary Conditions 13

3.2 Model Validation 14

3.3 Results Presentation 16

3.3.1 Porosity Variation 16

3.3.2 Lateral Pore Number Variation 18

3.3.3 Electrode Morphology Variation 20

3.3.4 Pressure Variation 22

3.3.5 Temperature Variation 26

4 CONCLUSIONS AND FUTURE PERSPECTIVES 31

4.1 Future Perspectives 32

5 BIBLIOGRAPHY 33

A. ANNEX 35

A.1 Thesis Model Corroboration 35

A.1.1 Thesis Model's Results using Butler-Volmer Equation 35

A.1.2 Ma *et al.* (2018) Replicated Model's Results (Adapted from the Thesis Model) 37

List of Figures

Figure 1.1: Artificial and Natural Photosynthesis. Image adapted from [10]. 1
Figure 1.2: Representation of an electrolyzer. Image adapted from [14]. 3
Figure 1.3: CO_2 Reduction. Image adapted from [20]. 5
Figure 2.1: Adapted from C. Ma *et al*. (2018), a 2D schematic representation of the porous quinone electrode considered in the computer model. Image adapted from [21]. 7
Figure 2.2: Presentation of the COMSOL Multiphysics working environment. 8
Figure 3.1: Flowchart of the optimization steps of the simulated porous zinc cathode's model. 16
Figure 3.2: Geometry of the porous zinc cathode, with porosity 0.30829. 17
Figure 3.3: Geometry of the porous zinc cathode, with porosity 0.88382. 17
Figure 3.4: Polarization curves for different porosities. 18
Figure 3.5: Model of the porous zinc cathode, *eps* = 0.69500 and n_i = 4. 18
Figure 3.6: Model of the porous zinc cathode, *eps* = 0.69500 and n_i = 8. 18
Figure 3.7: Polarization curves of different number of lateral pores "n_i", with porosity 0.69500. 19
Figure 3.8: Contour Plot of the porous zinc cathode considering circular shaped fibers. 19
Figure 3.9: Model of the porous zinc cathode, with circular fiber shape geometry, porosity 0.69500. 20
Figure 3.10: Model of the porous zinc cathode, with equilateral triangular fiber shape geometry, porosity 0.69500. 20
Figure 3.11: Model of the porous zinc cathode, with regular hexagonal fiber shape geometry, porosity 0.69500. 20
Figure 3.12: Model of the porous zinc cathode, with square fiber shape geometry, porosity 0.69500. 20
Figure 3.13: Polarization curves of different geometric fiber shapes with a lateral pore number of 3. 21
Figure 3.14: Polarization curves of different geometric fiber shapes with a lateral pore number of 4. 21
Figure 3.15: Equilateral triangular shape fiber's Contour Plot of the porous zinc cathode. 21
Figure 3.16: Regular hexagonal shape fiber's Contour Plot of the porous zinc cathode. 21
Figure 3.17: Square shape fiber's Contour Plot of the porous zinc cathode. 21
Figure 3.18: Polarization curves of different porosities at 5 bar. 23
Figure 3.19: Polarization curves for the different "n_i's", with porosity 0.79756 at 5 bar. 23
Figure 3.20: Polarization curves of different porosities at 10 bar. 23
Figure 3.21: Polarization curves for the different "n_i's", with porosity 0.79756 at 10 bar. 23
Figure 3.22: Polarization curves of different porosities at 15 bar. 24
Figure 3.23: Polarization curves for the different "n_i's ", with porosity 0.79756 at 15 bar. 24
Figure 3.24: Polarization curves of different porosities at 20 bar. 24
Figure 3.25: Polarization curves for the different "n_i's ", with porosity 0.79756 at 20 bar. 24
Figure 3.26: Circular shape fiber's Contour Plot of the porous zinc cathode at 5 bar. 25
Figure 3.27: Circular shape fiber's Contour Plot of the porous zinc cathode at 10 bar. 25
Figure 3.28: Circular shape fiber's Contour Plot of the porous zinc cathode at 15 bar. 25

Figure 3.29: Circular shape fiber's Contour Plot of the porous zinc cathode at 20 bar..... 25
Figure 3.30: Variation of CO_2 solubility in aqueous solutions with temperature. Extracted from [33]. 26
Figure 3.31: Polarization curves of different porosities at 1 bar and 45ºC. 27
Figure 3.32: Polarization curves for the different "n_i's", with porosity 0.79756 at 1 bar and 45ºC. 27
Figure 3.33: Polarization curves of different porosities at 20 bar and 45ºC. 27
Figure 3.34: Polarization curves for the different "n_i's", with porosity 0.79756 at 20 bar and 45ºC. 27
Figure 3.35: Polarization curves of different porosities at 1 bar and 70ºC. 28
Figure 3.36: Polarization curves for the different "n_i's", with porosity 0.79756 at 1 bar and 70ºC. 28
Figure 3.37: Polarization curves of different porosities at 20 bar and 70ºC. 28
Figure 3.38: Polarization curves for the different "n_i's", with porosity 0.79756 at 20 bar and 70ºC. 28
Figure 3.39: Circular shape fiber's Contour Plot of the porous zinc cathode at 1 bar and 45ºC. 29
Figure 3.40: Circular shape fiber's Contour Plot of the porous zinc cathode at 20 bar and 45ºC. 29
Figure 3.41: Circular shape fiber's Contour Plot of the porous zinc cathode at 1 bar and 70ºC. 29
Figure 3.42: Circular shape fiber's Contour Plot of the porous zinc cathode at 20 bar and 70ºC. 29
Figure 4.1: The different types of optimizations of the porous zinc cathode's model. 31
Figure A.1: Polarization curves for different porosities. 35
Figure A.2: Polarization curves for the different "n_i's" with porosity 0.68745. 35
Figure A.3: Polarization curves of different geometric fiber shapes with a lateral pore number of 3. 35
Figure A.4: Circular shape fiber's Contour Plot of the porous zinc cathode. 36
Figure A.5: Regular hexagonal shape fiber's Contour Plot of the porous zinc cathode. 36
Figure A.6: Square shape fiber's Contour Plot of the porous zinc cathode. 36
Figure A.7: Equilateral triangular shape fiber's Contour Plot of the porous zinc cathode. 36
Figure A.8: Polarization curves for different porosities. [21] 37
Figure A.9: Polarization curves for the different "n_i's" with porosity 0.6152. [21] 37
Figure A.10: Polarization curves of different geometric fiber shapes with a lateral pore number of 5. [21] .. 37

List of Tables

Table 3.1: CO_2R species transport and electrochemistry parameters. 12

Table 3.2: C. Ma *et al.* (2018) geometric parameters applied to the cathode employed by Luo *et al.* (2019). 14

Table 3.3: Operational parameters used in the validation of the zinc porous cathode's model. 14

Table 3.4: Geometric parameters of different porosities of the porous zinc cathode.[21][26] 16

Table 3.5: Different Diffusion Coefficients for each chemical species, depending on the inlet pressure. [32] 22

Table 3.6: CO_2 Solubilities in aqueous solutions according to the inlet pressure and the temperature. [33] .. 26

Symbols

Symbol	*Description*	*Units*
i	Chemical species index	---
c_i	Concentration of species i	mol/m^3
$c_{i,0}$	Initial concentration of species i	mol/m^3
C_R	Coefficients for the reduced species i	---
C_O	Coefficients for the oxidized species i	---
a_i	Chemical activity of species i	---
L_p	Channel length	m
d_f	Fiber diameter of the solid fibers	m
d_p	Pore length	m
L	Lateral length of the porous electrode	m
Z	Thickness of the porous electrode	m
S	Surface length	m
V	Electrolyte volume	m^2
A_V	Specific or volumetric area	1/m
n	Number of fibers/pores of the porous electrode	---
ne	Number of electrons exchanged in the CO_2 reduction reaction	---
n_i	Number of solid fibers per row/column	---
D_i	Diffusion coefficient of species i	m^2/s
z_i	Electric charge number of the species i	---
F	Faraday's constant	C/mol
R	Molar gas constant	J/mol.K m^3.Pa/mol.K
M	Molar mass	Kg/mol
i	Net current density	A/m^2
i_s	Current density at the electrode	A/m^2
i_l	Current density in the electrolyte	A/m^2
i_0	Negative exchange current density	A/m^2
i_{loc}	Local current density of species	A/m^2
T	Temperature	K
T_{ref}	Reference, or ambient, temperature (25°C)	K
p	Pressure	Pa
P_{ref}	Reference, or ambient, pressure (1 atm)	Pa
q	Volumetric flow rate	m^3/s
P_{in}	Inlet pressure	Pa
$Q_{V,out}/Q_{out}$	Outlet volume flow rate	m^3/s
E^0_i	Equilibrium standard potential of species i	V
$E_{eq,i}$	Equilibrium potential of the reduction reaction of species i	V
E_c	Applied potential (vs. RHE)	V
pH	Electrolyte pH	---

Symbol	*Description*	*Units*
K_f	Kinetic constant of the CO_2 reduction reaction	m/s
u	Fluid surface velocity vector	m/s
$\vec{n}$	Output unit normal vector	m/s
ν	Dynamic fluid viscosity	m^2/s
$\varepsilon/\varepsilon_l$	Volumetric porosity	---
σ/σ_s	Electrode electrical conductivity	S/m
σ_l	Electrolyte electrical conductivity	S/m
α_c	Cathodic transfer coefficient of CO_2	---
α_a	Anodic transfer coefficient of CO_2	---
Φ/Φ_s	Applied electric potential (vs. RHE)	V
η	Overvoltage (vs. RHE)	V
ρ	Electrolyte density	Kg/m^3
μ	Electrolyte kinematic viscosity	Pa.s
RHE	Reversible hydrogen electrode: $E^0_{H+} = E^0_{H+}$ (V vs. SHE) – 0.059 x pH	V
SHE	Standard hydrogen electrode: $E^0_{H+} = 0$ V (at any temperature)	V

Motivation

There is a large amount of energy in the sunlight that reaches earth, but it changes over time, dispersing, which makes it difficult to use it, however, it has been possible to successfully use solar energy to generate electricity, but it has not yet been possible to efficiently store it. The solar fuels approach investigated here can offer a cost-effective solution to this problem.

Solar fuels could diversify our fuel supply and increase the sustainability of our global energy system. They can be sent anywhere, making them valuable and versatile resources for a more reliable energy network. One possible approach to solar fuel production is the "artificial photosynthesis".

Artificial photosynthesis is a field of research that aims to mimic the natural photosynthesis of plants, using sunlight to convert carbon dioxide and water into carbohydrates and oxygen (see Figure 1).

This makes it an attractive technology not only from a practical and economic point of view, but also from an ecological point of view, as it could potentially help to mitigate or reverse some of the adverse effects produced by the consumption of fossil fuels, such as, for example, global warming.

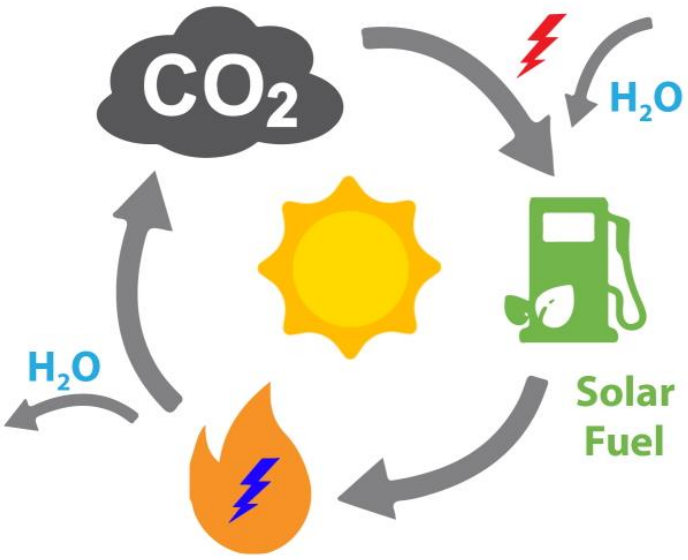

Figure 1: Schematic of the Solar Fuels concept. Image adapted from [1].

1 Introduction

Despite the benefits, the use of fossil fuels is associated with several environmental issues, namely problems such as global warming (which is, as we know, caused by the excess of CO_2 in the atmosphere), acid rain (originated from the reaction between pollutants and water vapor), as well as water contamination. [2]

The dependence of the world energy matrix on non-renewable energy sources means that the reservoir is constantly shrinking due to the intensive and unrestricted exploitation of natural resources. [3]

Due to the harmful consequences of the massive use of fossil fuels, human beings began to think of alternatives to replace those fuels, such as solar energy, which is obtained when the sun's natural energy is converted into electrical or thermal energy. The energy in question is generated in two ways: by converting sunlight into electricity or by converting the heat of sunlight into electricity. [4]

More recently, there has been a lot of talking and numerous studies made about the solar-powered processes with H_2O and CO_2 as basic power sources, which can produce "solar fuels", that can replace the non-renewable fuels already mentioned. [5]

However, because sunlight is unequally dispersed worldwide and is intermittent, intensive use of solar energy for human needs will require energy storage in high energy density fuels, like liquid hydrocarbons.

There is currently no practical and cost-effective technology to convert sunlight directly into useful fuels, which requires innovative technologies and novel studies.

Thinking of photosynthesis as the process by which the conversion of solar energy into chemical energy by the synthesis of organic compounds, provides a model for the storage of solar energy into fuels. Fossil energy consumed today comes from sunlight collected by photosynthetic organisms. [6][7]

In this way, artificial photosynthesis becomes a field of research that aims to mimic the natural photosynthesis of plants, which uses sunlight to convert carbon dioxide and water into carbohydrates and oxygen. [8]

Natural photosynthesis has dozens of enzymes that catalyze many individual reactions. However, the full process is conceptually divided into two major steps that interact via energy-carrying molecules, these being: photoreaction, which depends on sunlight, and the reaction in the dark, which can occur without light. These reactions are of foremost importance from a scientific and economic point of view, due to their potential application in the development of solar energy. However, the process is very complex and difficult to understand even in the laboratory. [8][9]

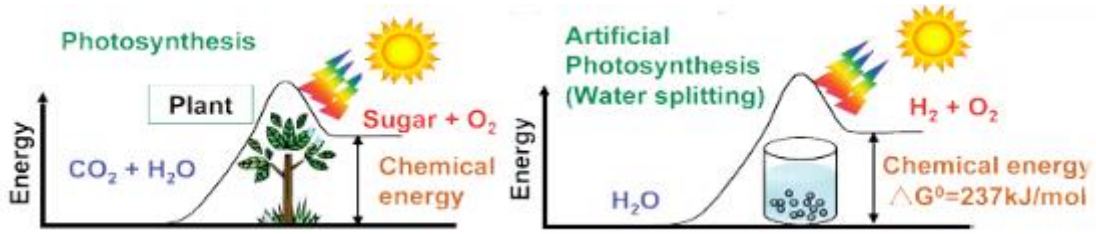

Figure 1.1: Artificial and Natural Photosynthesis. Image adapted from [10].

Artificial photosynthesis research applies the basic scientific principles of natural processes to the design of solar energy conversion systems. These technologies use varied materials, that scientists fine-tune, to produce energy efficiently and beneficially for human needs.

Three main components are required to produce fuels through natural or artificial photosynthesis. First, antenna/reaction center complexes absorb sunlight and convert the excitation energy into electrochemical (redox) energy. Second, a water oxidation complex uses this redox potential to catalyze the conversion of water into hydrogen ions, electrons stored as reductants, and oxygen. A second catalytic system uses the reductants to produce fuels, such as carbohydrates (e.g., methane), carbon monoxide (used to produce syngas), lipids, or hydrogen gas. [6]

These "solar renewable fuels" can potentially play a key role in future energy systems, both as a means of energy transport and as raw materials in the energy sector itself. In addition, they can become competitive alternatives to fossil fuels.

In an optimistic scenario, it is predicted that competitivity between the use of fossil fuels and renewable fuels for energy production can be achieved between 2025 and 2048, for all power generation channels. Two technologies have balanced costs for 2050, even in an extremely conservative baseline scenario: these are H_2 production by water electrolysis and diesel production by Fischer-Tropsch synthesis. Both technologies use solid oxide electrolysis, which benefits from rapid cost reduction and has shown to be highly efficient. [11]

Consequently, we have the production of hydrogen through electrolysis of water, as an endothermic energy process, which takes place by consumption of electrical energy. The core of where the electrolysis occurs is an electrochemical cell, which is filled with pure water and has two electrodes connected to an external power supply. At a certain voltage, which is called the critical voltage, between both electrodes, they start producing hydrogen gas at the negatively polarized electrode and oxygen gas at the positively polarized electrode. The amount of gas produced per unit of time is directly related to the current passing through the electrochemical cell. [12]

Electricity in excess supplied from renewable energy resources, such as wind and solar energy, can also be used for electrolysis, which produces green H_2. In addition, fluctuations in renewable energy systems can be minimized by storage.

The most common and developed techniques used in hydrogen electrolysis are alkaline, proton exchange membrane (PEM), and solid oxide electrolysis cells (SOEC). [13]

The alkaline electrolyzers work by transferring hydroxide ions (OH^-) through the electrolyte from the cathode to the anode, meanwhile producing hydrogen gas on the cathode side. An electrolyte that uses a liquid alkaline solution of sodium hydroxide, or potassium hydroxide, as the electrolyte has been on the market for many years. These commercialized electrolyzers (efficiency of approximately 73%) can achieve 380.000 kg of H_2 per year, with a system energy consumption of 53.4 kWh per kg H_2, costing EUR 3.15 per kg. [13]

In the second technology discussed, PEM, the electrolyte is a solid polymeric material where water reacts at the anode to form oxygen and positively charged hydrogen ions (protons). The electrons flow through an external circuit and the hydrogen ions moves selectively through the PEM to the cathode. In terms of hydrogen produced per unit of electricity utilized to drive the reaction, PEM electrolysis has an electrical efficiency of around 80% in functioning use. PEM electrolysis efficiency is predicted to reach 82-86% by 2030.

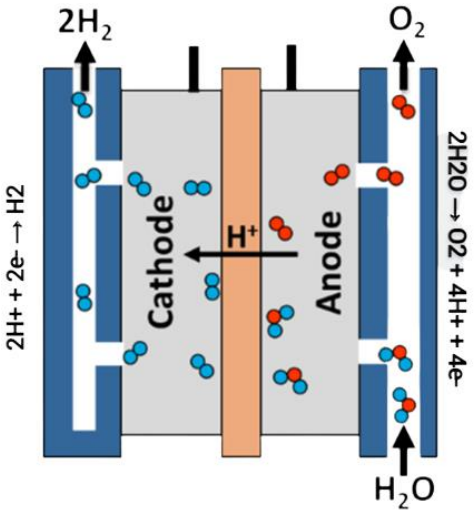

Figure 1.2: Representation of an electrolyzer. Image adapted from [14].

Anode Reaction: $2H_2O \leftrightarrow O_2 + 4H^+(aq) + 4e^-$ (Eq. 1)

Cathode Reaction: $2H^+(aq) + 2e^- \leftrightarrow H_2(g)$ (Eq. 2)

In the case of the solid oxide electrolyzers (SOEC), the hydrogen is produced in a slightly different way, as they use a solid ceramic material as an electrolyte, which selectively conducts the negatively charged oxygen ions (O_2^-) at elevated temperatures.

Next, this work will focus on explaining the Fischer-Tropsch Synthesis (FTS) in more detail, and what this second technique (already mentioned above) consists of.

Fischer-Tropsch Synthesis (FTS) is strongly considered an option to the production of clean fuels and chemicals. FTS is a process that uses a catalyst to convert syngas into a variety of hydrocarbons. The C-O bond is broken, allowing the carbon and the hydrogen to react with the molecular hydrogen to form hydrocarbons, water, and, to a lesser extent, carbon dioxide. All these characteristics attract the interest of people (mainly industries) all over the world. [5][15]

Franz Fischer himself was aware of the importance of his discovery, which supplied a path to industrial organic chemistry based on simple inorganic molecules. His finding might be of utmost relevance now, when fossil fuel use must be discontinued to avoid irreversible climate changes.

The performance of the FTS depends strongly on the reaction temperature. The increase in temperature will favor the selective formation of methane, and will favor also the deposition of carbon and, therefore, the deactivation of the catalyst. [15]

After this, and now talking more in-depth about the carbon dioxide gas, and some of the methodologies around CO_2 capture and/or utilization, it is common knowledge that one of the most serious environmental problems today is related to the impact of CO_2 emissions, a gas that is responsible for about 60% of the greenhouse effect that plagues our planet, and which remains in the atmosphere for hundreds of years.

Nowadays, harnessing CO_2 from industrial emissions is seen as a way to complement other strategies to reduce CO_2 emissions, such as the use of renewable energy sources.

Carbon capture and storage (CCS) is a process in which CO_2, before entering the atmosphere, is transported, and stored (carbon sequestration) for centuries or millennia in natural underground geological structures, such

as caves or depleted water reservoirs. In addition to this technology, there are other low-carbon technologies [16].

Key opportunities for CO_2 use include recycling CO_2 without conversion (e.g., enhanced oil recovery, supercritical CO_2) or converting CO_2 into valuable fuels, energy storage media, or chemicals.

Among the CO_2 conversion technologies, such as biochemical, photosynthetic, thermocatalytic and photocatalytic processes, electrochemical CO_2 reduction (CO_2R) is a suitable process for electrolyzers with mild operating conditions. It has great potential as a CO_2-based technology because it can be operated at moderate operating conditions (ambient temperature and near-atmospheric pressure) in electrolyzers; because of the ability to control the selectivity of reaction products simply by controlling the applied potential/current density; because of the potential use as an electrolyte for industrial or municipal wastewater; and because of the modular reactor design. Also, the CO_2R can be combined with carbon-intensive industries, integrating renewable solar and wind power and carbon recycling processes. [7][17][18]

The first major challenge of CO_2R is its excessive cost, as quite the amount of energy needed to break the bonds of the CO_2 molecule. The next challenge is to achieve high selectivity of CO_2 among the desired products, to minimize the cost and complexity of the products separation processes. [17]

Achieving high selectivity is difficult because of the several CO_2R reactions competing with the hydrogen evolution reaction (HER), all of which have equilibrium potentials (E0) in a narrow range (0.25 V to 0.17 V, compared to the Standard Hydrogen Electrode (SHE)). [17]

The third task, in this CO_2R chapter, is to ensure that the overall reaction rate is not limited by the mass transfer rate of CO_2 from the gas phase to the electrolyte, and by the trapped areas of the cathode catalyst. [17]

A fourth practical challenge is maintaining the electrocatalyst's stable performance over a long period of operation, because the catalyst can be poisoned by impurities in the electrolytes or in the O_2 feed gas (e.g., sulphur compounds). [17]

Another major problem in the electrochemistry of CO_2 reduction is related to the interaction between CO_2 and water. A complex series of reversible reactions occur when CO_2 is introduced into an aqueous environment. The relative proportions of these compounds can be adjusted by pH, as an increase in pH will lead to an increase in the number of dissolved carbonates in the solution. Although this appears to be a quick and easy way to obtain high concentrations of aqueous CO_2 solutions, it is generally accepted that dissolved CO_2 is the only species that can be electrochemically reduced at metal electrodes, not the carbonate species. [17]

The electrochemical reduction of CO_2 in solid-state catalysts involves the interaction between the adsorbed CO_2 molecule, the electron, and the proton. For this reduction to occur, the CO_2 molecules obtain protons or electrons on the electrode surface. The whole reaction process contains three steps [19]:

i. The adsorption of CO_2;
ii. The surface diffusion of CO_2 and the transformation of the electron and proton into CO_2;
iii. The desorption of the products.

The adsorption of CO_2 on the surface of the solid catalyst is a key step in the whole reaction. During the adsorption process, the C=O bond is highly disrupted by the substrate, and electrons are shared between CO_2 and the catalyst. [19]

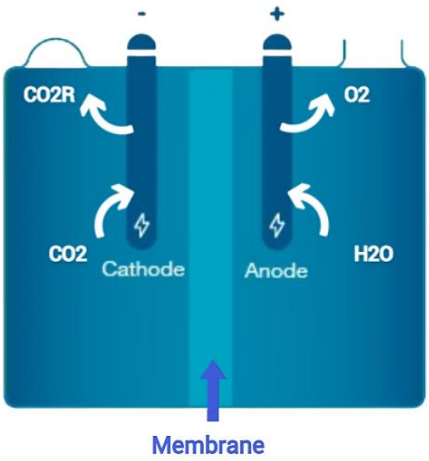

Figure 1.3: CO_2 Reduction. Image adapted from [20].

The CO_2 reduction reaction process could be a 2, 4, 6, or 8 electrons process, which will produce CO, $HCOOH$, $HCHO$, CH_3OH or CH_4, respectively: [19]

$$CO_2 + 2H^+ + 2e^- \rightarrow CO + H_2O \qquad E^0 = 0.52\,V \qquad \text{(Eq. 3)}$$

$$CO_2 + 2H^+ + 2e^- \rightarrow HCOOH \qquad E^0 = 0.61\,V \qquad \text{(Eq. 4)}$$

$$CO_2 + 4H^+ + 4e^- \rightarrow HCHO + H_2O \qquad E^0 = 0.51\,V \qquad \text{(Eq. 5)}$$

$$CO_2 + 6H^+ + 6e^- \rightarrow CH_3OH + H_2O \qquad E^0 = 0.38\,V \qquad \text{(Eq. 6)}$$

$$CO_2 + 8H^+ + 8e^- \rightarrow CH_4 + 2H_2O \qquad E^0 = 0.24\,V \qquad \text{(Eq. 7)}$$

$$CO_2 + 12H^+ + 12e^- \rightarrow C_2H_4 + 4H_2O \qquad E^0 = 0.34\,V \qquad \text{(Eq. 8)}$$

The rate-limiting step of the reaction is strongly influenced by the properties of the catalyst, such as the metal surface, the oxidation state of the surface and its crystalline structure. [19]

This study is one more significant step ahead in developing a consistent technology for CO_2 electroreduction since it will allow us to reduce CO_2 emissions to the atmosphere while also providing a viable source of renewable fuels powered by electricity derived from solar energy. It also allows the conversion of CO_2 into compounds that can be utilized as raw materials in the creation of diverse products such as plastics, solvents, fuels, and medications, CO_2 electroreduction on a zinc cathode has been suggested as a possible solution for reducing greenhouse gas emissions. However, many obstacles must be solved before this technology can be widely used as a viable solution for lowering greenhouse gas emissions. The key obstacles include expanding the process's efficiency and scale, as well as lowering the expenses connected with its implementation.

In this work, a 2D model of porous electrodes developed by C. Ma *et al.* (2018), for the design of quinone-based electrodes for continuous-flow batteries is suitable for designing and optimizing porous electrodes for the joint carbon dioxide-hydrogen and water electrolysis using zinc cathodes. That said, we used the previously mentioned model as a basis, by making some necessary modifications, to adapt it to the simulation of the desired operation conditions, chemical reactions, and electrode morphology. [21]

To replicate this, we used COMSOL Multiphysics® software to simulate the model developed and analyzed in this Master Thesis. This is the same program used by C. Ma *et al.* (2018). [21]

The biggest advantage of using a porous electrode is the ability to obtain a large surface area, thus increasing the efficiency of the catalyst electrode.

2 Materials and Methods

In this thesis, a two-dimensional porous electrode model developed by C. Ma *et al.* (2018) on the design of electrodes for quinone-based flow batteries was adapted to allow the design and optimization of porous electrodes in their electrolyte for the co-electrolysis of CO_2 and water using a porous zinc cathode. [21]

To do this, the COMSOL Multiphysics® program was used on a computer where a 2D reference electrode structure was built on, where the electrochemical reactions, which occur in the interface electrode/electrolyte as the electrolyte travels through the electrode pores, were simulated.

Since 1998, COMSOL has marketed technical modelling and simulation software that enables the design and analysis of electrical, mechanical, fluid, and chemical applications. [22]

This company fundamental part on this field is COMSOL Multiphysics®, which models and simulates physical phenomena using advanced numerical methods. In terms of compatibility with other tools, the software is adaptable and can be used in conjunction with CAD and MATLAB, for example. This ensures that aspects such as geometry, mesh, settings and boundary conditions can be easily managed. [22]

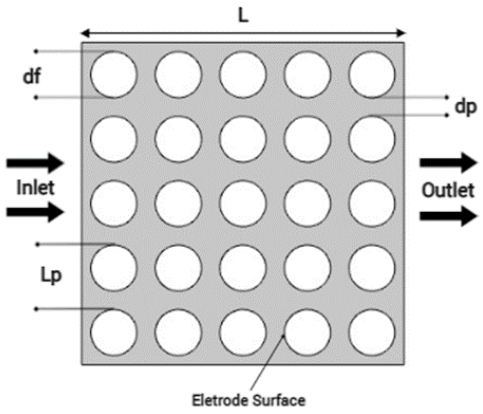

Figure 2.1: Adapted from C. Ma *et al.* (2018), a 2D schematic representation of the porous quinone electrode considered in the computer model. Image adapted from [21].

Figure 2.1 depicts the model's shape, where d_p denotes the pore diameter ("pore channel") and d_f denotes the fibre diameter of the solid electrode. To facilitate the reader's perception, the circles indicate the circular fibers that comprise the solid electrode (solid phase); the space between the circles symbolizes the "porous channel" through which the electrolyte flows (liquid phase). [21]

In the figure directly below (Figure 2.2) you can get a sense of how the COMSOL Multiphysics's working environment is. On the left side, we have displayed everything that is being varied and studied. You can access the basic parameters ("Parameters 1"), the components of what is being studied, for example, the geometry of the electrode, the materials and settings needed for the program to "run" correctly (to "compute", in the software's terminology). A little further down, you can also see the implementation modules: Secondary Current distribution, Transport of Diluted Species and Creeping Flow.

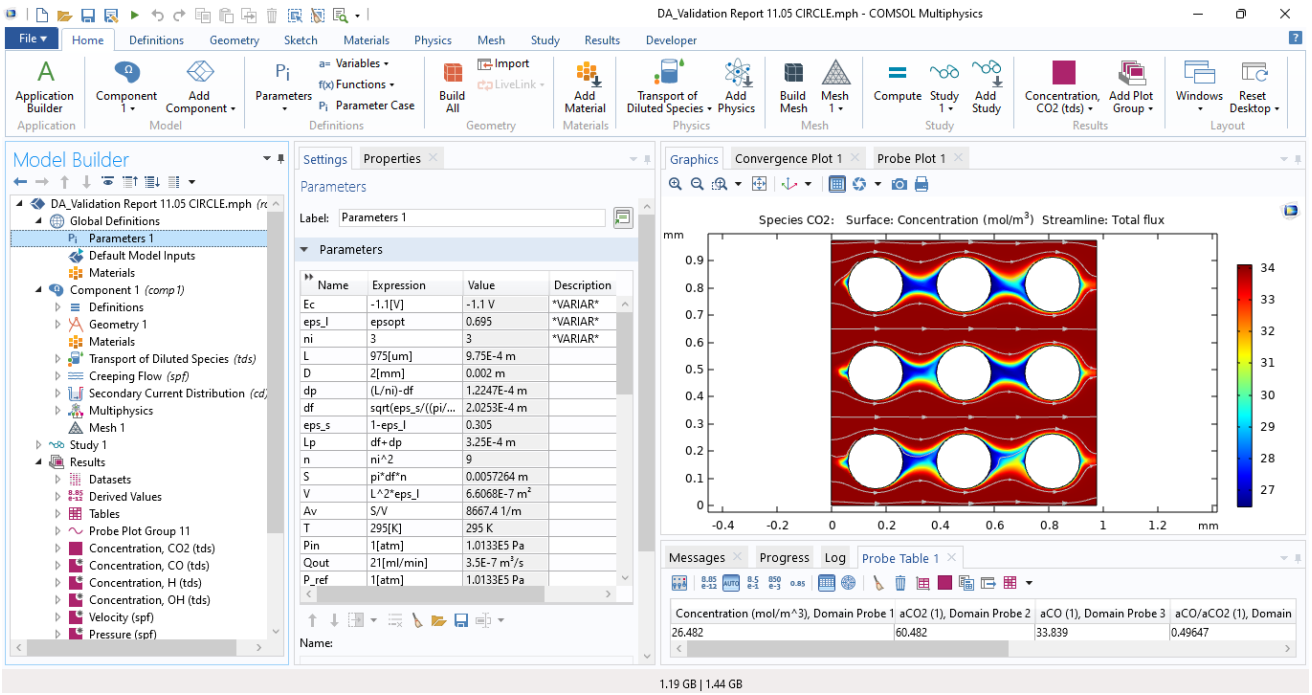

Figure 2.2: Presentation of the COMSOL Multiphysics working environment.

To further describe each of these implementation modules, the Secondary Current Distribution (cd) considers the effect of electrode kinetics, as well as the resistance of the solution. The electrolyte composition and behavioral assumptions are the same as for the primary current distribution, resulting in Ohm's law for the electrolytic current. The primary and secondary current distributions differ according to the description of the electrochemical process at the interface of an electrolyte and an electrode. [23]

The Creeping Flow (spf) interface is used to simulate fluid flows at extremely low Reynolds numbers, allowing the inertial term in the Navier-Stokes equations to be ignored. Creeping flow, also known as Stokes flow, occurs in high viscosity or small geometrical length scale systems (for example, in microfluidics and MEMS devices). The fluid might be compressible or incompressible, Newtonian, or non-Newtonian. [24]

The Chemical Species Transport Branch's Transport of Diluted Species (tds) interface is used to compute the concentration field of a dilute solute in a solvent. This interface can oversee the transport and interactions of species dissolved in a gas, liquid or solid. Diffusion by Fick's law, convection when coupled to a flow field and migration when coupled to an electric field can all be driving forces for transport.[25]

The interface allows for the simulation of convection and diffusion transport in 1D, 2D, and 3D, as well as axisymmetric components in 1D and 2D. The molar concentration, c, is the dependent variable. Multiple species transit can be modelled, with the physics interface solving for the molar concentration, c_i, of each species i. [25]

3 Results and Discussion

3.1 Model Description and Geometry

Some mathematical expressions were defined initially for the characterization and implementation of this model, which was needed for the further computations of this modelling process in COMSOL Multiphysics® Software.

The lateral dimension of the porous electrode (porous cathode, in this case) is denoted as L(m), and the overall electrode area is L^2 (L *x* L, m^2). [21]

We also define L_p (m) as the distance between the solid particles (fibers), i.e., between the two maximum limits of d_f (m). As a result, according to the expression [21]:

$$d_p = L_p - d_f \quad \text{(Eq. 9)}$$

The value of d_p (m) may be calculated using the values of L_p (m) and d_f (m), and by using n_i, the latter reflecting the number of lateral fibers (side solid particles of the electrode). As seen in the following formula, the greater the value of n_i, the lower the value of d_p (m) [21]:

$$d_p = \frac{L}{n_i} - d_f \quad \text{(Eq. 10)}$$

Another calculation of the lateral dimension of the porous cathode L (m) is shown below. Remembering that L_p (m) is the distance between electrode's solid fibers [21]:

$$L = n_i L_p = n_i(d_p + d_f) = n_i \times d_p + n_i \times d_f \quad \text{(Eq. 11)}$$

The value of n stands for the total number of solid particles (fibers) of the electrode present in our porous cathode. Therefore, you must multiply the number of fibers (n_i) you have on each side (as an example, consider Figure 2.1) [21]:

$$n = n_i^2 \leftrightarrow n = 5^2 \leftrightarrow n = 25 \quad \text{(Eq. 12)}$$

The solid fibers of the electrode's surface length is calculated by multiplying the number of fibers by their diameter and the Pi number [21]:

$$S = d_f \times n \times \pi \quad \text{(Eq. 13)}$$

The electrode porosity (ε) is defined by the following expression [21]:

$$\varepsilon = 1 - \frac{\pi}{4} \times d_f^2 \times \frac{n}{L^2} \quad \text{(Eq. 14)}$$

$V\,(m^2)$ is the definition of pore volume per unit of height as following [21]:

$$V = \varepsilon \times L^2 \qquad \text{(Eq. 15)}$$

The specific or volumetric area, $A_V\,(m^{-1})$, is the quotient of the surface length of the solid fibers of the electrode, S (m), and the volume of the electrolyte contained in the porous cathode, $V\,(m^2)$, as shown in the next expression [21]:

$$A_V = \frac{S}{V} \leftrightarrow \frac{d_f \times n \times \pi}{\varepsilon \times L^2} \leftrightarrow \frac{d_f \times ni \times \pi}{ni^2 \times L_p^2 \times \varepsilon} \leftrightarrow \frac{\pi \times d_f}{ni(d_f + d_p)^2 \varepsilon} \qquad \text{(Eq. 16)}$$

3.1.1 Model Purposes

As previously said, the electrochemical reduction of CO_2 will occur in the porous cathode according to the equation:

$$CO_2(g) + 2H^+(aq) + 2e^- \leftrightarrow CO(g) + H_2O(l) \qquad \text{(Eq. 17)}$$

And the reduction of the proton (in an acidic electrolyte) is given by the equation:

$$2H^+(aq) + 2e^- \leftrightarrow H_2(g) \qquad \text{(Eq. 18)}$$

This porous electrode system is particularly complex since it is composed of highly non-linear variables and intricate partial differential equations that combine fluid dynamics with electrochemical processes in the porous electrode model (such as diffusion, migration, and convection of the electrically charged species that generate the electrode electric current and control its performance).

Some simplifying assumptions about species transport had to be created to simulate such a complex electrochemical system:

I. Isotropic and homogenous electrode materials are used. [21]
II. The electrolyte is seen as an incompressible fluid with isothermal flow and is treated as a Stokes fluid ("creeping flow," with the Reynolds Number substantially lesser than 1, $Re \gg 1$). [21]
III. The effects of gravity are not considered. [21]
IV. It is assumed that the process is in a stationary state. Because the modelling solution modes in COMSOL® are classified into two categories: time-dependent and stationary state, there is no relationship between time and the reaction kinetic process in this model. [21]
V. All pores have maximum efficiency. Because all pore channels are connected in this model and there is no fluid stagnation zone, the electrode availability is 100%. [21]
VI. This 2D geometry model will never be able to fully reflect the porous zinc cathode's 2D geometrical structure, which has a 3D structure with irregular straight-section pores. For modelling purposes, the geometric approximation employed in this 2D reference model will be circles, which represent cylindrical zinc solid fibers of the electrode. [21]

3.1.2 Mathematical Model Development

3.1.2.1 Fluid Flow Model

The flow distribution across the porous cathode's channels is captured using a 2D laminar flow model, and the pressure drop across the electrode is calculated using the well-known Navier-Stokes equations [21]:

$$\nabla \times \mathrm{u} = 0 \quad \text{(Eq. 19)}$$

$$(u \times \nabla) \times \mathrm{u} + \frac{1}{\rho}\nabla \mathrm{p} - \nu \times \nabla^2 u = 0 \quad \text{(Eq. 20)}$$

Where u is the superficial fluid velocity vector (m/s), p is the pressure in the liquid, ρ is the electrolyte density (Kg/m^2), and v is the dynamic viscosity (m^2/s).

3.1.2.2 Mass Transport and Electrochemical Model

The governing equations for species conservation and charge conservation in the electrolyte in this model are as follows [21]:

$$D_i \times \nabla^2 c_i - \nabla \times \left(\frac{D_i z_i c_i}{RT}\right)\nabla\phi + u * \nabla c_i \quad \text{(Eq. 21)}$$

The balances and equations supplied below will be used to model the electrochemical processes occurring in the porous cathode.

Because the electrolyte is electrically neutral, it is governed by the condition [21]:

$$\sum_i z_i c_i = 0 \quad \text{(Eq. 22)}$$

The Conservative Balance of Electrical Current Density occurs when the charge entering the electrolyte i_l (A/m^2) is balanced by the charge exiting the solid phase i_s (A/m^2), which equals the net current density i (A/m^2), as can be seen in the following equation [21]:

$$\nabla \times i_l = -\nabla \times i_s = \nabla \times i \quad \text{(Eq. 23)}$$

The following equations (Equations 24 and 25) represent the electrolyte current density i_l (A/m^2) and conductivity σ_l (S/m) where D_i (m^2/s) is the diffusion coefficient in solution for species i. The z_i stands for the species charge number, F represents Faraday's constant (F = 96485 C/mol), T represents temperature (K), and R represents the molar gas constant (R = 8.3145 J/mol.K). Meanwhile, the electrolyte potential ϕ_l (V) and the electrode potential ϕ_s (V) submit to Ohm's Law (Equations 26 and 27, being σ_s (S/m) the electrode conductivity:

$$i_l = F\sum_{i=1}^{n} z_i\,(-D_i - \sigma_l \nabla \phi_l) \quad \text{(Eq. 24)}$$

$$\sigma_l = \frac{F^2}{RT}\sum_{i=1}^{n} z_i^2 D_i c_i \quad \text{(Eq. 25)}$$

$$i_l = -\sigma_l \nabla \phi_l \quad \text{(Eq. 26)}$$

$$i_s = -\sigma_s \nabla \phi_s \quad \text{(Eq. 27)}$$

The Nernst Equation is utilized on the porous electrode surface to calculate the equilibrium potential of the governing electrochemical processes, where E_{eq} (V) is the negative electrolyte's equilibrium potential. *R* is the molar gas constant (J/mol.K), *T* is the temperature (K), *F* is Faraday's constant (C/mol), and *ne* is the number of electrons exchanged in the reaction (*ne* = 2 in this case [26]). This equation can be seen below [21]:

$$E_{eq,CO_2} = E^0_{CO_2} + \frac{RT}{ne * F}\, ln\left(\frac{a_{CO_2}}{a_{CO}}\right) \quad \text{(Eq. 28)}$$

The Linearized Butler-Volmer Equation describes the electrochemical reactions that occur on the surface of the porous electrode and calculates the transfer current densities for the reactions that happen there. Where i_0 is the exchange current density (A/m^2) for the electrode, η is the over-voltages (V) for the electrode, α_a (anodic) and α_c (cathodic) are the transfer coefficients. *F* stands for the Faraday's constant (C/mol) and *R* for the molar gas constant (J/mol.K), as always. This expression is the following [21]:

$$i_{loc} = i_0\left(\frac{(\alpha_a + \alpha_c)F}{R\,T}\right)\eta \quad \text{(Eq. 29)}$$

The Coefficients for the Reduced Species C_R, which is CO in the CO_2 reduction reaction (Equation 30), and for the Oxidized Species C_O, which is CO_2 for the present case (Equation 31), are presented below, being a_{CO} (mol/m^3) the chemical activity of the CO species, and a_{CO_2} (mol/m^3) the chemical activity of the CO_2:

$$C_R = a_{CO} \quad \text{(Eq. 30)}$$

$$C_O = a_{CO_2} \quad \text{(Eq. 31)}$$

For the application of the Equations previously stated, the values of the Species Transport and Electrochemical Constants, needed for the modelling of the porous zinc cathode in the COMSOL® Software, are available in the following table:

Table 3.1: CO_2R species transport and electrochemistry parameters.

Designation	***Symbol***	***Value***	***Units***	***Bibliographic Sources***
Electrode Conductivity	σ_s	16.6×10^6	S/m	[27]
CO_2 Diffusion Coefficient	D_{CO_2}	1.92×10^{-9}	m^2/s	[28]
CO Diffusion Coefficient	D_{CO}	2.03×10^{-9}	m^2/s	[28]
H^+ Diffusion Coefficient	D_{H^+}	9.31×10^{-9}	m^2/s	[21]
OH^- Diffusion Coefficient	D_{OH^-}	5.27×10^{-9}	m^2/s	[26]
Standard Potential of CO_2 vs. RHE	$E^0_{CO_2}$	0.73037	V	[26][29]

Designation	*Symbol*	*Value*	*Units*	*Bibliographic Sources*
CO_2 Exchange Current Density	i_0	68.1	A/m^2	Optimized
CO_2 Kinetics Constant	K_f	*Variable*	m/s	[26]
CO_2 Transfer Coefficient (Cathodic)	α_c	0.5	---	[30]
CO_2 Transfer Coefficient (Anodic)	α_a	1.5	---	[30]
Electrolyte Density	ρ	1×10^3	Kg/m^3	[30]
Electrolyte Kinematic Viscosity	μ	1×10^{-3}	Pa.s	[30]

3.1.3 Model Boundary Conditions

Equation 32 is useful for discussing the boundary conditions. In this study, we analyse stationary-state simulation; the concentration along the y-direction is symmetric at the top and bottom borders and the species fluxes are zero [21]:

$$N \times \vec{n} = 0 \begin{cases} 0 \le x \le L, y = 0 \\ 0 \le x \le L, y = L \end{cases} \quad \text{(Eq. 32)}$$

The pressure equation follows (save at the inlets and outlets), in which a Neumann condition is applied at every domain of the boundaries of integration [21]:

$$\nabla \mathrm{p} \times \vec{n} = 0 \quad \text{(Eq.33)}$$

At the inlet, the boundary condition states that each species enters with a specified bulk concentration and a velocity determined by the pump rate [21]:

$c_i = c_{i,0}$ ($c_{i,0}$ is the initial concentration of *i* species at the inlet) (Eq. 34)

$p = P_{in}$ (P_{in} is the pressure at the inlet) (Eq. 35)

At the outlet, the boundary condition is defined as [21]:

$-\vec{n} * D_i \nabla c_i = 0$ (where $\vec{n}$ expresses the outward unit normal vector) (Eq. 36)

$q = Q_{out}$ (Q_{out} is the volumetric flow at the outlet) (Eq. 37)

Electric current flows in and out of the electrolizer via the two current collectors at the upper end of the zinc porous cathode and the anode. The voltage at the negative current collector is swept for half-cell modelling [21]:

$\phi_s = E_c$ (Applied at the interfaces between solid fibers and electrolyte) (Eq. 38)

3.2 Model Validation

Another of the main goals of this thesis is to translate the experimental results of Luo *et al.* (2019) into a COMSOL® Software's model, to obtain the corresponding simulation results in terms of Electrochemistry, i.e., Polarization Curves, allowing the direct comparison with the results of the article previously mentioned in this paragraph.

To validate this model, Luo *et al.*'s geometric parameters, as well as their operational conditions, must be input into the COMSOL Multiphysics® Software.

The research by Luo *et al.* (2019) is an experimental work so, with the goal of creating a simulation like that created by C. Ma *et al.* (2018), it was next essential to geometrically approximate the two models: define pore length (dp), electrode side length (or portion thereof, L) and number of solid fibers visible on the electrode (or portion thereof) per row or column (n_i). These data are presented in the following tables (Table 3.2 and Table 3.3):

Table 3.2: C. Ma *et al.* (2018) geometric parameters applied to the cathode employed by Luo *et al.* (2019).

Designation	***Symbol***	***Value***	***Units***	***Bibliographic Source***
Pore length	d_p	80	µm	[26]
Fiber diameter of the solid fibers	d_f	245	µm	Estimated from [26]
Number of solid fibers per row/column	n_i	3	---	[26]
Lateral length of the porous electrode	L	975	µm	Estimated from [26]
Thickness of the porous electrode	Z	2	mm	[26]

Table 3.3: Operational parameters used in the validation of the zinc porous cathode's model.

Description	***Symbol***	***Value***	***Units***	***Bibliographic Source***
Operating Temperature	T	295.00	K	[26]
Inlet Pressure	P_{in}	1	atm	[26]
Outlet Volumetric Flow	Q_{out}	21	mL/min	[26]
Initial CO_2 Concentration	$c_{CO_2,0}$	34	mol/m^3	[26]
Initial CO Concentration	$c_{CO,0}$	0	mol/m^3	[26]
Initial H^+ Concentration	$c_{H^+,0}$	1.6 x 10^{-4}	mol/m^3	Estimated from [26]
Initial OH^- Concentration	$c_{OH^-,0}$	6.3 x 10^{-5}	mol/m^3	Estimated from [26]
Electrolyte pH	pH	6.8	---	[26]
Applied Potential vs. RHE	E_c	-1.5 to -0.5	V	[26]
Reference Temperature	T_{Ref}	298.15	K	PTN
Reference Pressure	P_{Ref}	1	atm	PTN

In the ANNEX A.1.1 we show the Polarization Curve plots of the present Thesis' Model using the Butler-Volmer Equation, instead of the Linearized Butler-Volmer Equation, which was used for the rest of the simulations previously shown in this work, for corroboration purposes. The process was the same: optimization of porosities as shown in Figure A.1, in Annex and optimization of the lateral number of pores (from 2 to 8), as shown in Figure A.2. [31]

After that, the best porosity and lateral number of pores was taken, and the best fiber shape geometry of the cathode was found to apply to this model. As with the Linearized Butler-Volmer Equation, the best fiber shape was the equilateral triangle and the square, with their current density values remarkably close (see Figure A.3). [31]

As it was done in the present Thesis, after the Polarization Curves study, the Contour Plots were studied and one can observe similarities between the previously studied ones, and the ones presented in the figures below, not only graphically but also in terms of the current density values obtained in both models. [31]

With these parallel studies, there is a general corroboration of the Thesis Model's results and a verification that the differences in the current density values between one model and the other, using the Linearized Butler-Volmer Equation, or the Non-Linearized Equation, do not differ much in magnitude (from Figure A.4 to Figure A.7). [31]

In the ANNEX A.1.2, what was done was to use the model created in this Thesis and to replicate the main results of the model of Ma *et al.* (2018).

When it comes to porosities, it did not vary substantially (the best porosity is 0.4973, just like in the authors' report). The best geometry in the model of Ma *et al.* (2018) was also the equilateral triangular fiber shape (which also aligns with the Ma *et al.*'s finds), but in this case the square fiber shape no longer shares such close values to the first geometry mentioned (as occurs with the present Thesis model). The most significant difference was in the number of lateral pores, being the present work's best "n_i" 3 or 4, and the article's 9, but that can be explained by the multitude of differences between the geometric characteristics and the operational conditions of each model. [25]

After this, it can be stated that there is further corroboration between the model studied in this Thesis and that one of Ma *et al.* (2018), because the results of the previous report can be simulated by the Thesis model with a remarkable accuracy (Figure A.8, Figure A.9 and Figure A.10).

3.3 Results Presentation

This Master Thesis has several optimization steps, each of which is dependent on the earlier one. Figure 3.1, shown below, provides a detailed summary of the steps taken during the project.

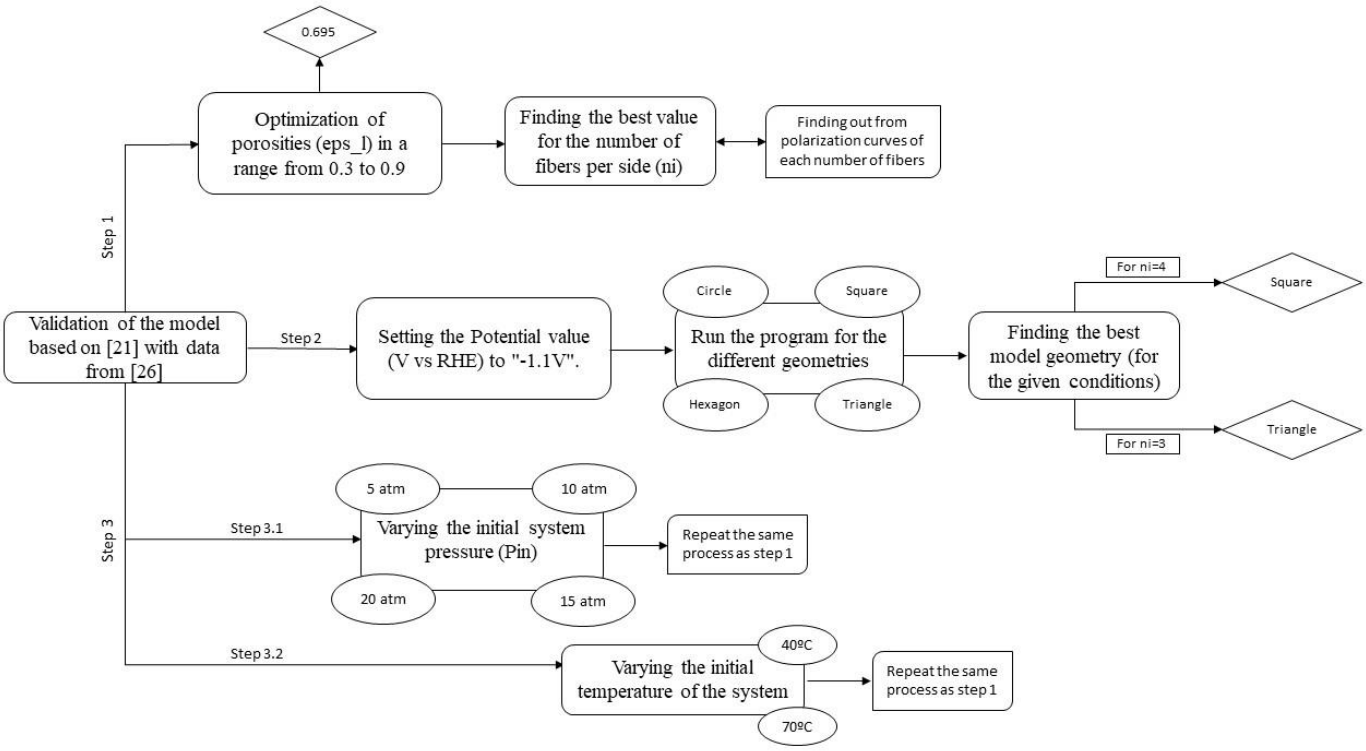

Figure 3.1: Flowchart of the optimization steps of the simulated porous zinc cathode's model.

3.3.1 Porosity Variation

The current subsection investigates the variation of porosity of the geometrical structures in the model simulations of the porous zinc cathode, using the Linearized Butler-Volmer Equation. The figures below show the differences in cathode geometry when the porosity is 0.30 (Figure 3.2) and when it is 0.80 (Figure 3.3). Where it can also be seen that with the variation of porosity, there is variation of pore length (d_p), fibre diameter (d_f) and surface length (S).

Table 3.4: Geometric parameters of different porosities of the porous zinc cathode.[21][26]

Porosity, ε	**Fiber diameter, d_f (m)**	**Pore length, d_p (m)**	**Surface length, S (m)**	**Lateral pore number (n_i)**
0.30829	3.05×10^{-4}	2.00×10^{-5}	8.26×10^{-3}	3
0.39603	2.85×10^{-4}	4.00×10^{-5}	8.05×10^{-3}	3
0.47783	2.65×10^{-4}	6.00×10^{-5}	7.49×10^{-3}	3
0.55367	2.45×10^{-4}	8.00×10^{-5}	6.92×10^{-3}	3
0.62357	2.25×10^{-4}	1.00×10^{-4}	6.36×10^{-3}	3
0.68751	2.05×10^{-4}	1.20×10^{-4}	5.79×10^{-3}	3

Porosity, ε	Fiber diameter, d_f (m)	Pore length, d_p (m)	Surface length, S (m)	Lateral pore number (n_i)
0.69500	2.03×10^{-4}	1.22×10^{-4}	5.72×10^{-3}	3
0.74551	1.85×10^{-4}	1.40×10^{-4}	5.23×10^{-3}	3
0.79756	1.65×10^{-4}	1.60×10^{-4}	4.67×10^{-3}	3
0.84366	1.45×10^{-4}	1.80×10^{-4}	4.10×10^{-3}	3
0.88382	1.25×10^{-4}	2.00×10^{-4}	3.53×10^{-3}	3

The figures below show the difference in pore size between the lowest investigated porosity and the highest studied porosity.

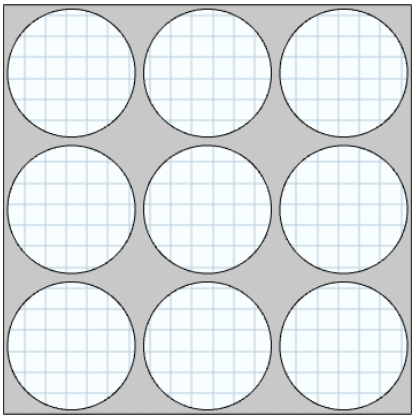

Figure 3.2: Geometry of the porous zinc cathode, with porosity 0.30829.

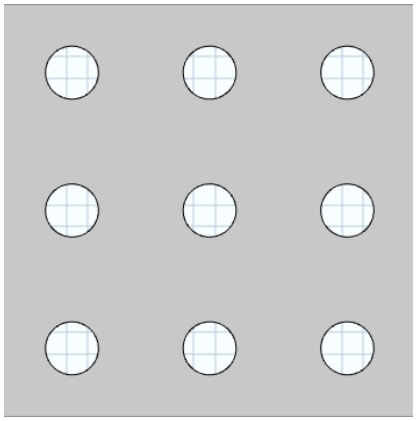

Figure 3.3: Geometry of the porous zinc cathode, with porosity 0.88382.

For the study of the porosities, it was used a function of the COMSOL® Software that is the "Optimization (opt)" Module. For such, it was chosen an analytical method named Nelder-Mead, which requires an initial value of porosity, and a final value of porosity, with a step of 0.0001, which demonstrates how thorough will be our study, to find the maximum value of current density for the cathode's geometry of n_i = 3. It was also necessary to choose an applied potential to conduct this analytical method study. So, the applied potential set was -1.10 V vs. RHE, because it is the maximum applied potential studied by Luo *et al.* (2019), the one at which the current density in that paper reaches its limit value, and therefore the current density associated with that potential (45 mA/cm^2), from the reference and model validation paper in this thesis, is the one considered as the reference value for comparison in the studies of cathode geometry, temperature and pressure.

Besides the Optimization (the best value for porosity was *eps* = 0.69500), we studied the "behavior" of more 10 porosities (*eps* = 0.30829, *eps* = 0.39603, *eps* = 0.47783, *eps* = 0.55367, *eps* = 0.62357, *eps* = 0.68751, *eps* = 0.74551, *eps* = 0.79756, *eps* = 0.84366 and *eps* = 0.88382), as a mean of comparison to effectively understand if the Optimization process was correct.

As a way of carrying out this study, the following Polarization Curves were made, which are the graphs of the current densities ($i_{loc}, mA/cm^2$) as functions of the respective applied potentials (E_c, V vs. RHE), in the range of -1.50 to -0.50 V (vs. RHE), arising from the reduction reaction of CO_2-to-CO, for each of the cathode's geometric structures built, with the porosities previously mentioned. In the figure below, we can observe the "behavior" of the different porosities in this model and the respective current density associated with each of the porosities.

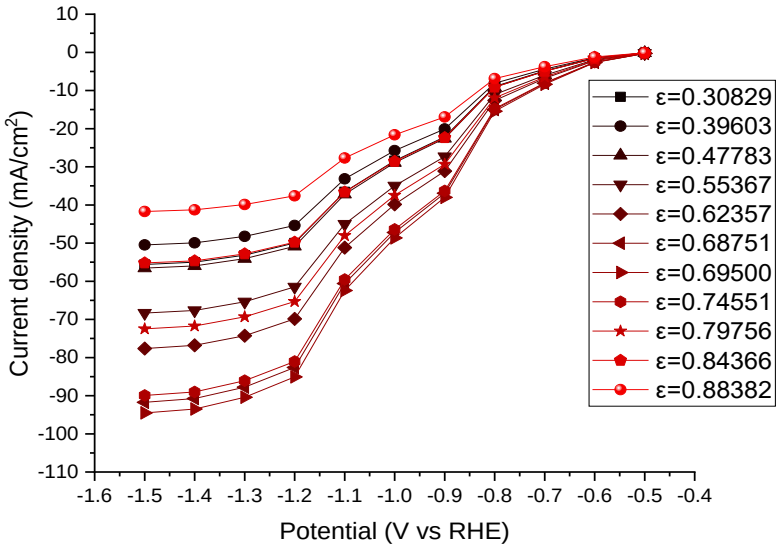

Figure 3.4: Polarization curves for different porosities.

3.3.2 Lateral Pore Number Variation

In this subsection, the number of pores per side was optimized. Under the same conditions as for the porosity, that is, with the applied potential from -1.50 to -0.50 V (vs. RHE), and in this case, already with the optimized porosity (0.69500). In the figure below we can see how the arrangement of the studied cathodes look with n_i = 4 and n_i = 8.

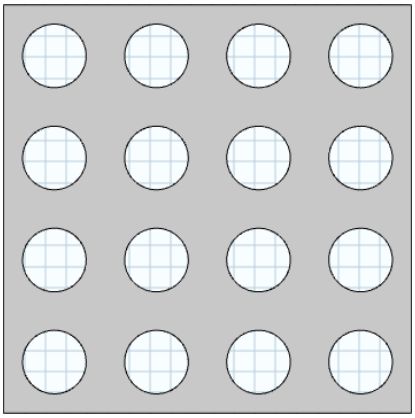

Figure 3.5: Model of the porous zinc cathode, *eps* = 0.69500 and n_i = 4.

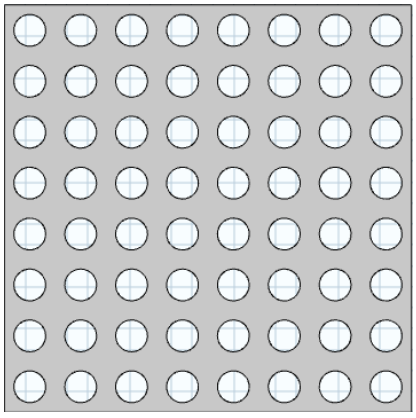

Figure 3.6: Model of the porous zinc cathode, *eps* = 0.69500 and n_i = 8.

Repeating the process already used in the porosity variation, we create again the Polarization Curves, where we have the current density ($i_{loc}, mA/cm^2$) in function of the applied potential (-1.50 to -0.50 V vs. RHE), and from these 8 curves, we realize that for this porosity the best n_i is 4, as we can see in the figure presented next.

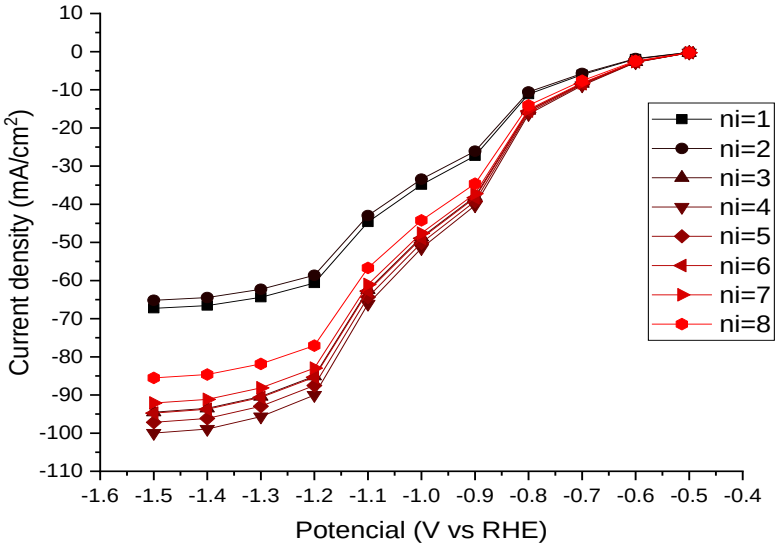

Figure 3.7: Polarization curves of different number of lateral pores "n_i", with porosity 0.69500.

To validate both polarization curves, a Contour Plot is utilized (of the porosities and of the number of lateral pores). This type of map is created by using the "Parametric Sweep", which is a COMSOL® Software function, in which we automatically change both the porosity (*eps* with a range from 0.3 to 0.9, with a step of 0.01) and the number of lateral pores (n_i with a range from 2 to 8, with a step of 1 unit). In this case, the applied potential set was -1.10 V vs. RHE, for the reasons already discussed before.

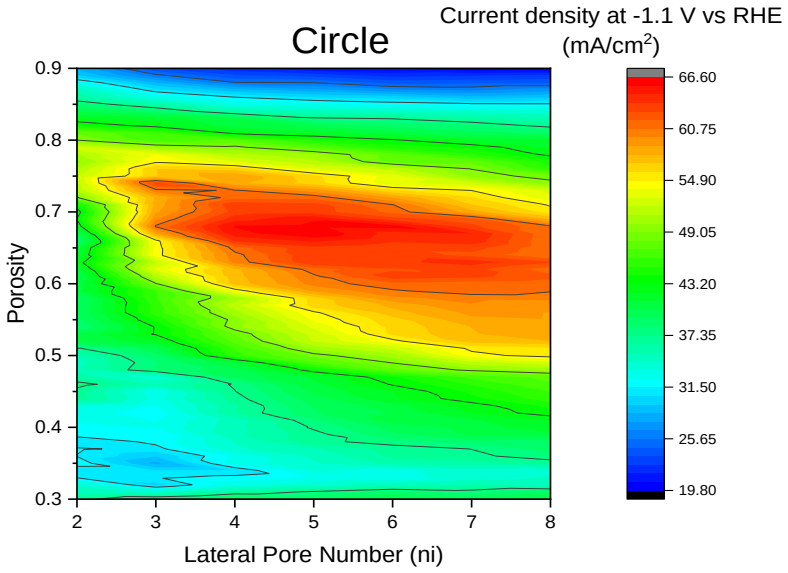

Figure 3.8: Contour Plot of the porous zinc cathode considering circular shaped fibers.

As can be seen above, the highest value of current density obtained in absolute terms is 66.60 mA/cm^2, and in this map we can also see that the highest values of current density are obtained between the porosity values of 0.6 and 0.7, and with more intensity between the values of n_i from 3 to 5. From there, the results disperse a little and are not as concentrated, as shown in Figure 3.8.

3.3.3 Electrode Morphology Variation

In the present section, the aim is to optimize the cathode's geometry to understand which geometrical fiber shape (among regular hexagonal, circular, equilateral triangular and square) is the best, i.e., which corresponds to the highest current density in absolute value. From Figure 3.9 to Figure 3.12are represented the different geometric fiber shapes that were studied. All 4 models have the same pore length, d_p, surface length, *S*, fiber diameter, d_f, and the same porosity, *eps* = 0.69500 (the optimized porosity for n_i = 3, as seen before).

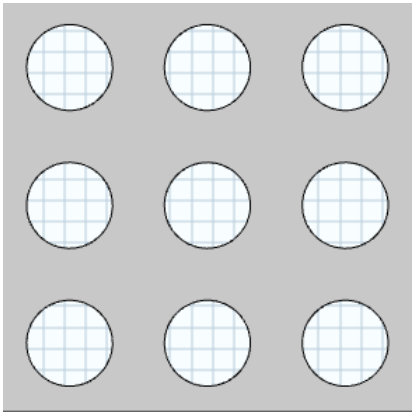

Figure 3.9: Model of the porous zinc cathode, with circular fiber shape geometry, porosity 0.69500.

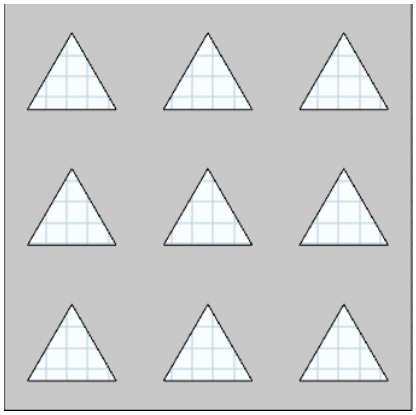

Figure 3.10: Model of the porous zinc cathode, with equilateral triangular fiber shape geometry, porosity 0.69500.

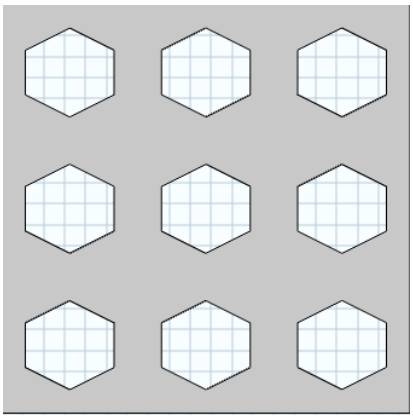

Figure 3.11: Model of the porous zinc cathode, with regular hexagonal fiber shape geometry, porosity 0.69500.

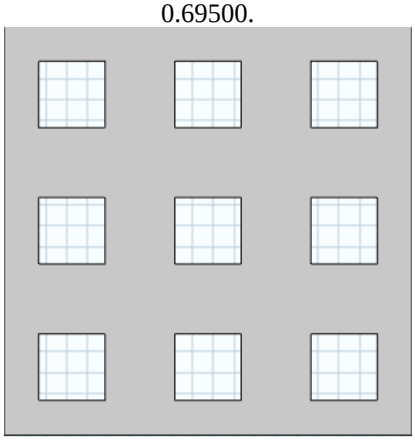

Figure 3.12: Model of the porous zinc cathode, with square fiber shape geometry, porosity 0.69500.

To do this study, the same methods were used to optimize the porosity and the lateral pore number (n_i). In this case, with fixed porosity (*eps* = 0.69500). In the case of the "n_i", it was varied between 3 and 4, to understand if there were any differences between the best geometric fiber shape and the worst, to realize if those differences were caused by changing the "n_i", in these simulations of the model of the porous zinc cathode.

The figures below show the behavior of each fiber geometry and the differences that exist between them. When n_i = 3, the equilateral triangle is the geometric fiber shape with the best performance, and the circle is the geometric shape with the worst behavior. On the other hand, when you have n_i = 4, the circle performs slightly better than the regular hexagon, and the square is the geometric fiber shape with the best performance in this situation. It should also be observed that the first example has a significantly higher current density than the second, particularly in the cases of square and equilateral triangle fiber shapes, as shown in Figure 3.13 and Figure 3.14.

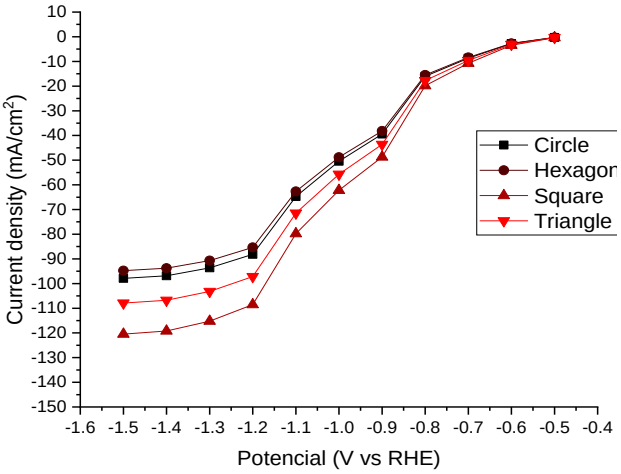

Figure 3.13: Polarization curves of different geometric fiber shapes with a lateral pore number of 3.

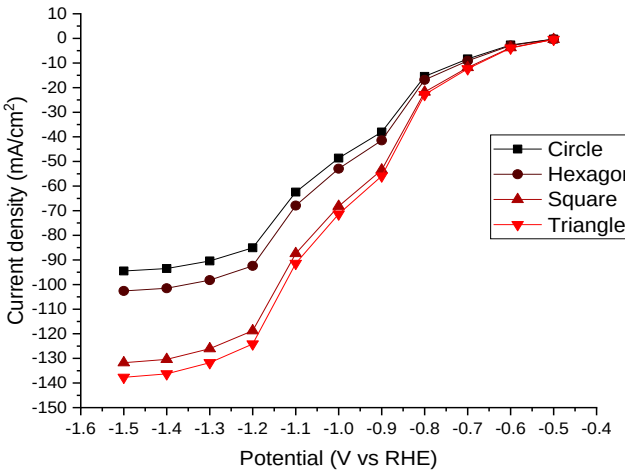

Figure 3.14: Polarization curves of different geometric fiber shapes with a lateral pore number of 4.

Following the previous Polarization Curves study for the various fiber shape geometries and the two "n_i's" studied (3 and 4), we return to the same procedure used in the cathode's circular fiber shape geometry study, the use of Contour Plots. This study had the same constraints as the one with the circular shape geometry, with porosity range from 0.3 to 0.9 (except for the hexagon, which had a range of 0.4 to 0.9), and a step of 0.01. The number of lateral pores varied from 2 to 8, with a step of 1 unit, for the next three geometries. These three graphs are depicted in the figures below (Figure 3.15, Figure 3.16 and Figure 3.17).

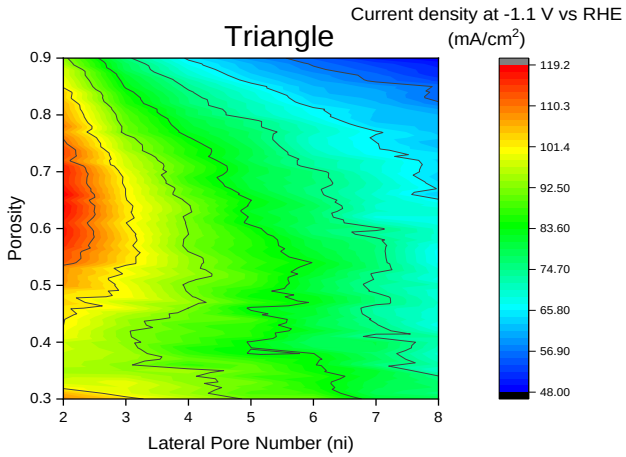

Figure 3.15: Equilateral triangular shape fiber's Contour Plot of the porous zinc cathode.

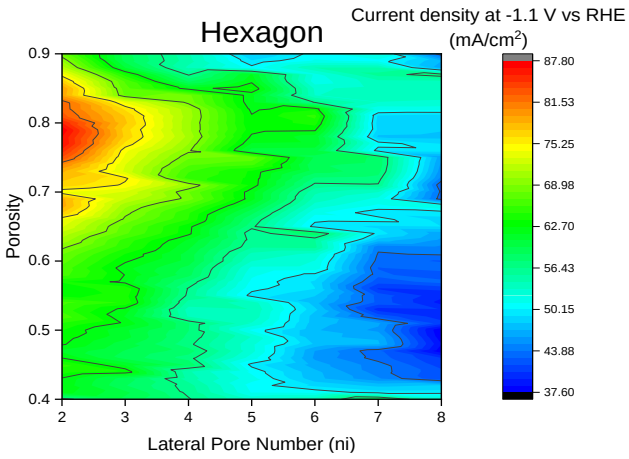

Figure 3.16: Regular hexagonal shape fiber's Contour Plot of the porous zinc cathode.

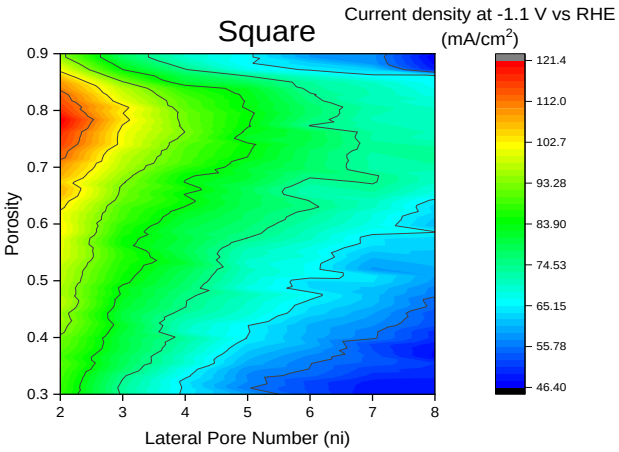

Figure 3.17: Square shape fiber's Contour Plot of the porous zinc cathode.

The examination of each figure shows that the best "n_i" for the three different fiber shape geometries is 2 or 3 number of lateral pores. The changes appear only when the porosity value is considered. In the equilateral triangular shape fiber, the red area, which corresponds to a higher current density, has a greater "diversity" of values. In this situation, the ideal porosity is around 0.3, but it can potentially range between 0.5 and 0.7.

The regular hexagonal fiber shape scenario differs from the preceding one in the way that the values are visibly more concentrated and not as spread, in comparison to the equilateral triangular fiber shape. The ideal porosity for this scenario is between 0.75 and 0.8.

Finally, we have the square fiber shape geometry, which behaves similarly to the hexagon, in the way that the values are more concentrated, but the optimum porosity is comprehended between 0.7 and 0.85.

If one looks at the maximum current density values in general, one finds the same order as in Figure 3.13, with the porous zinc cathode's square fiber shape geometry having an absolute maximum current density value of 121.4 mA/cm^2 and the equilateral triangular fiber shape having 119.0 mA/cm^2.

3.3.4 Pressure Variation

In this subsection, the study done is based on changing the Inlet Pressure (P_{in}). Keeping all the initial operational conditions of the previous studies the same, the initial pressure (P_{in} = 1 atm) was changed to 4 different values (5, 10, 15 and 20 bar).

For this study, it was necessary to find the diffusion coefficient (DC_i, m^2/s) values suitable for each pressure. Using the following equations, we calculated the density of each of the dissolved gases in the electrolyte for each inlet pressure [32]:

$$\rho = \frac{P \times M}{R \times T} \quad \text{(Eq. 39)}$$

$$\frac{DC_{p1}}{DC_{p2}} = \frac{\rho_{p2}}{\rho_{p1}} \quad \text{(Eq. 40)}$$

To find the value of each one of these densities (ρ, Kg/m^3) for each desired pressure (R = 0.0082 L.atm/mol.K), we know that M corresponds to the molar mass (Kg/mol), P to the pressure (atm) and T to the temperature (K), then we simply go to the Diffusion Coefficients formula (Equation 40) and find the coefficient for the desired pressure. After all these calculations completed, the following values were achieved, which can be consulted in the following table (Table 3.5):

Table 3.5: Different Diffusion Coefficients for each chemical species, depending on the inlet pressure. [32]

Pressure (bar)	***Pressure (atm)***	***CO_2 Diffusion Coefficient (m^2/s)***	***H^+ Diffusion Coefficient (m^2/s)***	***CO Diffusion Coefficient (m^2/s)***	***OH^- Diffusion Coefficient (m^2/s)***
1	0.98692	1.92×10^{-9}	9.31×10^{-9}	2.03×10^{-9}	5.27×10^{-9}
5	4.9346	$3.84 * 10^{-10}$	1.86×10^{-9}	4.06×10^{-10}	1.05×10^{-9}
10	9.8692	1.92×10^{-10}	9.31×10^{-10}	2.03×10^{-10}	5.27×10^{-10}
15	14.804	1.28×10^{-10}	6.21×10^{-10}	1.35×10^{-10}	3.51×10^{-10}
20	19.739	9.60×10^{-11}	4.66×10^{-10}	1.02×10^{-10}	2.63×10^{-10}

The common process that has been followed until now is completed after tabulating the updated values of Diffusion Coefficients in COMSOL® Software. To begin the studies, we must create the Polarization Curves of the different cathode geometries, both to discover the best porosities and to find the best "n_i's" (you must first know the best porosity to fix it and then get the best "n_i"). In this case, the 11 porosities, previously used in the initial study, were not used, but 5 of those 11 were chosen to perform the present study.

The 8 figures provided bellow (4 for porosity and 4 for the relevant "n_i's") show that there is a consistent tendency in all pressures. The reader may easily deduce that the optimal porosity for the 4 pressures is 0.79756, which corresponds to the green line with inverted triangles. At the same time, it is easy to understand that even when the pressure is highly increased, there is no significant increase in the current density value, which remains at approximately 90 mA/cm^2, in absolute value.

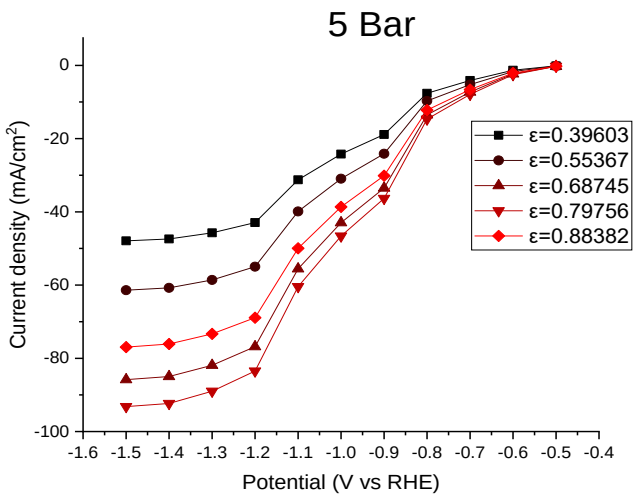

Figure 3.18: Polarization curves of different porosities at 5 bar.

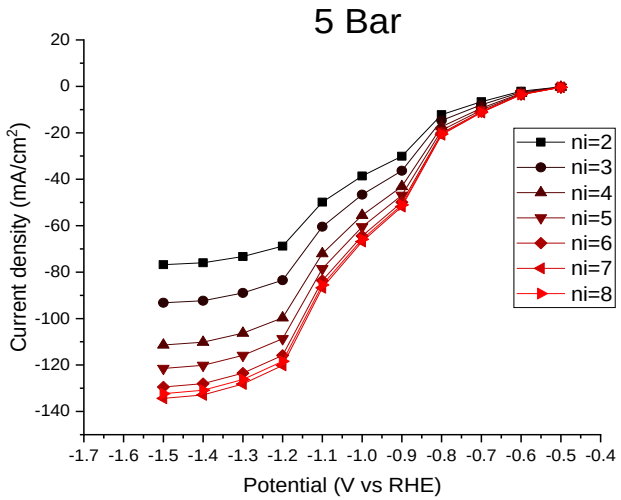

Figure 3.19: Polarization curves for the different "n_i's", with porosity 0.79756 at 5 bar.

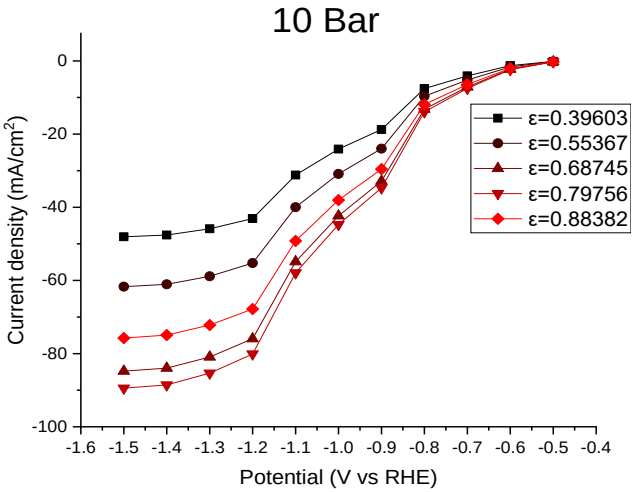

Figure 3.20: Polarization curves of different porosities at 10 bar.

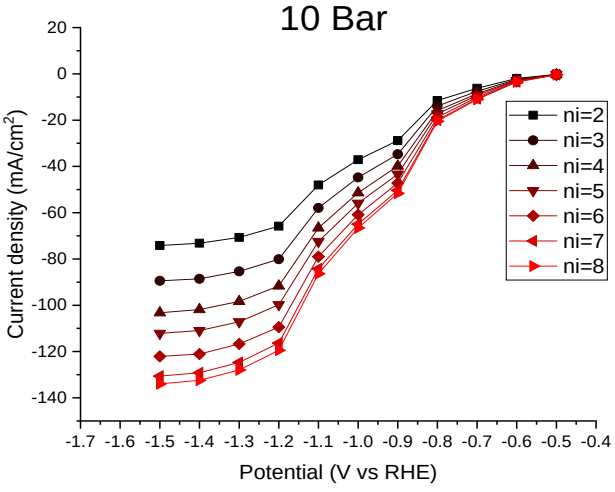

Figure 3.21: Polarization curves for the different "n_i's", with porosity 0.79756 at 10 bar.

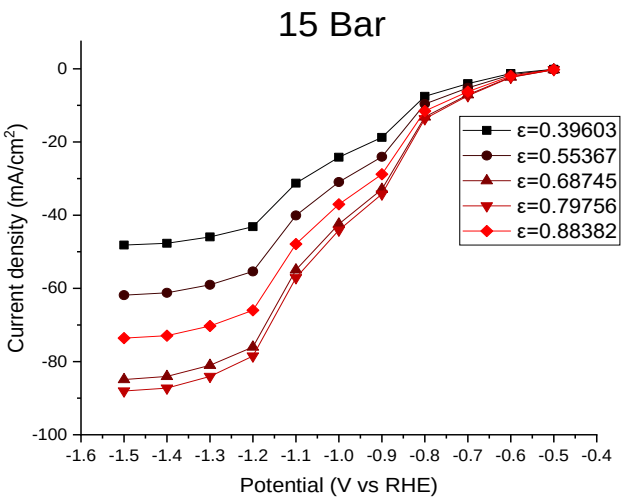

Figure 3.22: Polarization curves of different porosities at 15 bar.

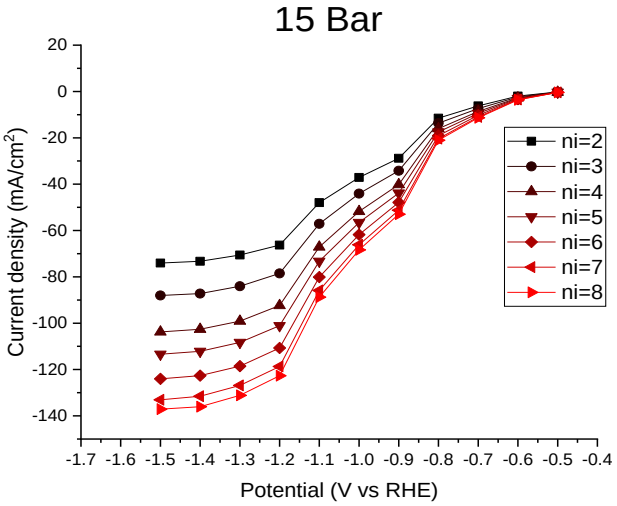

Figure 3.23: Polarization curves for the different "n_i's ", with porosity 0.79756 at 15 bar.

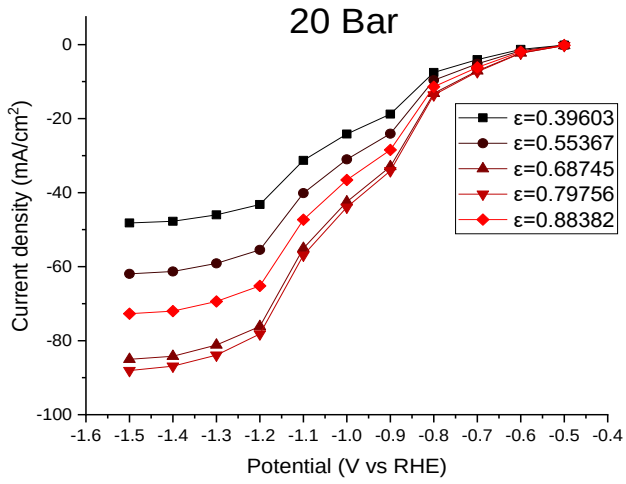

Figure 3.24: Polarization curves of different porosities at 20 bar.

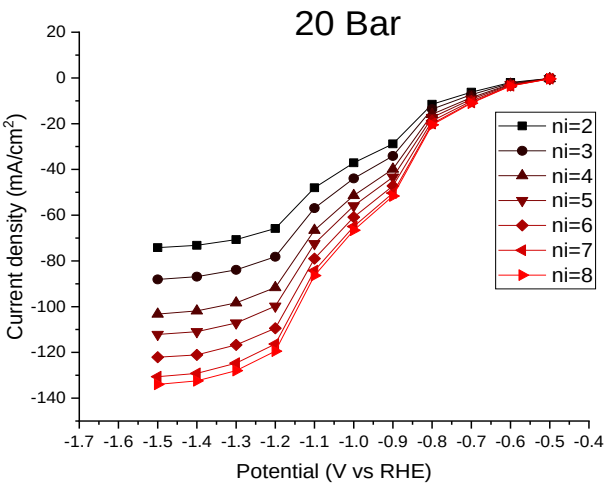

Figure 3.25: Polarization curves for the different "n_i's ", with porosity 0.79756 at 20 bar.

In terms of lateral pore number (n_i), as with porosity, the best n_i for these conditions is 8, apart from the first figure (Figure 3.26), where the pressure is of 5 bar and the best n_i is 7. However, the variation in current density is not substantial when n_i is 7 or 8, which have almost similar values, as illustrated in the next four graphics. Furthermore, as observed with the porosity studies, there was no significant increase in the current density with the increasing of pressure: in the four pressures analyzed, it was found to be around 140 mA/cm^2 (in absolute value) in all of them, for their circular geometries with the best performances.

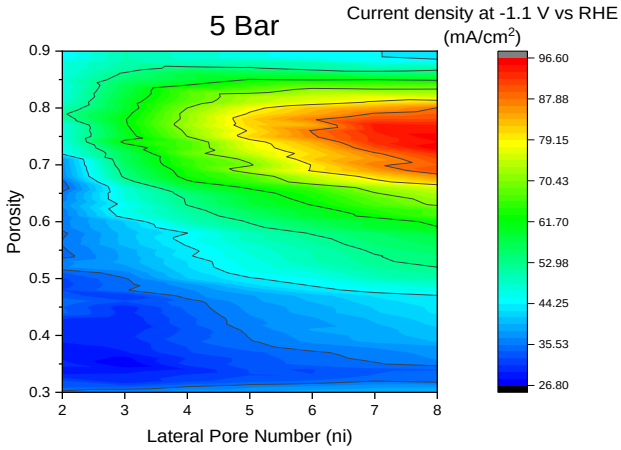

Figure 3.26: Circular shape fiber's Contour Plot of the porous zinc cathode at 5 bar.

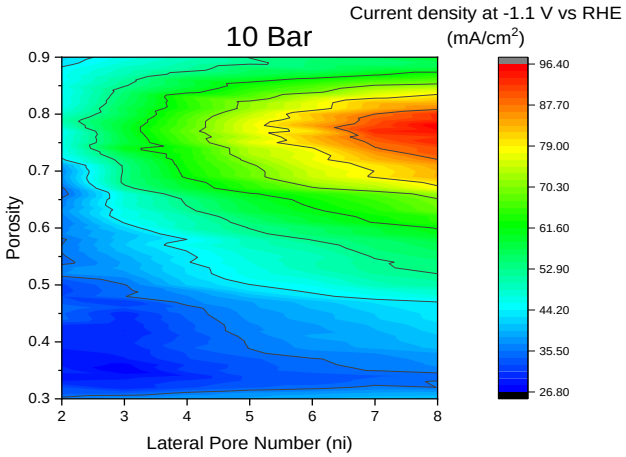

Figure 3.27: Circular shape fiber's Contour Plot of the porous zinc cathode at 10 bar.

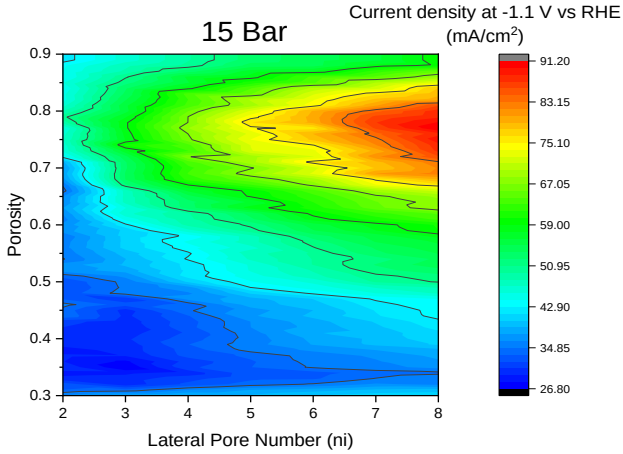

Figure 3.28: Circular shape fiber's Contour Plot of the porous zinc cathode at 15 bar.

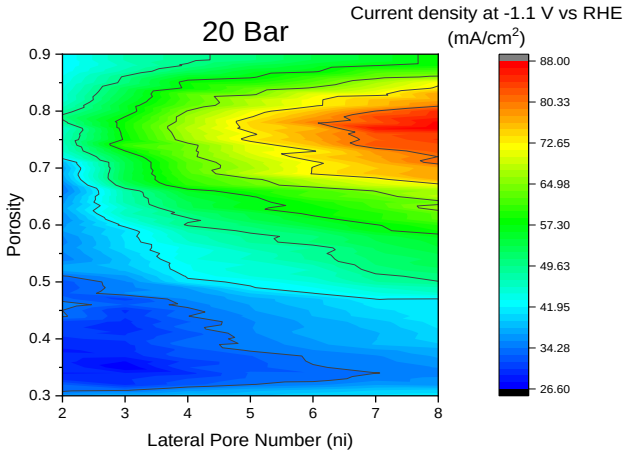

Figure 3.29: Circular shape fiber's Contour Plot of the porous zinc cathode at 20 bar.

After performing the study of the Polarization Curves, we must proceed to the Contour Plots analysis, as we have done previously. Using the exact same conditions as before (a "Parametric Sweep" of a porosity range of 0.3 to 0.9, with a step of 0.01 and, in the case of the "n_i", a range of 2 to 8, with a step of 1 unit). The results for the various pressures are homogeneous in these 4 figures. As seen in the study of the Polarization Curves, the best porosity is comprehended between the values of 0.7 and 0.8, and the best values for "n_i" are 7 or 8 pores per side.

Looking more closely at the current density values, we can see from the figures that the current density is better around 5 and 10 bar. Despite their proximity, the readings at 5 and 10 bars approach 96.47 mA/cm^2 and 96.34 mA/cm^2, respectively (in absolute value). The values at 15 and 20 bar are slightly lower, 91.20 mA/cm^2 and 88.00 mA/cm^2, respectively (in absolute value). As a conclusion, there is no need for a significant increase in pressure, or in the consequential energy consumption of the process, to optimize this porous zinc cathode's circular shape fiber geometry.

3.3.5 Temperature Variation

It was important to determine the new CO_2 solubility values for the corresponding Temperature and Inlet Pressures for this investigation of temperature variation. The figure below was essential for the following determinations of CO_2 solubilities in aqueous solutions (like the used electrolyte, which runs across the modeled porous zinc cathode):

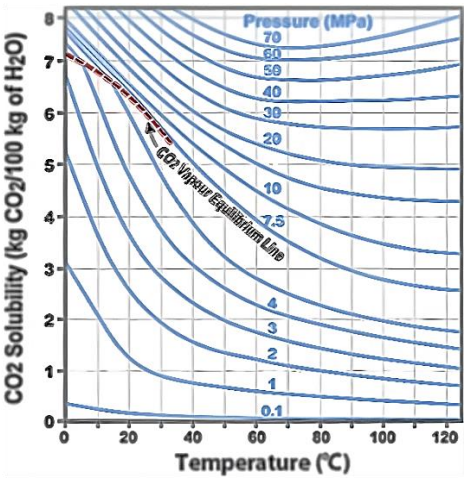

Figure 3.30: Variation of CO_2 solubility in aqueous solutions with temperature. Extracted from [33].

After having taken the necessary values of the CO_2 solubility in aqueous solutions at different inlet pressures and temperatures, the following table was formulated and inserted in the COMSOL® Software in an "Interpolation" Table, to define the CO_2 initial concentration at the inlet boundary ($c_{CO_2,0}$, mol.m^{-3}), to allow further studies on the temperature:

Table 3.6: CO_2 Solubilities in aqueous solutions according to the inlet pressure and the temperature. [33]

Temperature (K)	***Temperature (°C)***	***Inlet Pressure (atm)***	***Solubility ($g\ CO_2/100\ g\ H_2O$)***
295.00	22	1.0000	0.13990
293.15	20	1.0000	0.15026
298.15	25	1.0000	0.12953
318.15	45	1.0000	0.09845
343.15	70	1.0000	0.04145
343.15	70	19.739	5.0881
318.15	45	19.739	5.6536

Then, as on prior occasions, the identical optimization research was performed. First, there was the usual study of the Polarization Curves, which show us which are the best porosity and the best "n_i". The porosities for this study were the same as those used for the pressure variation study (0.39603, 0.55367, 0.68745, 0.79756 and 0.88382) and the "n_i" values were also the same used until now (from 2 to 8, with a step of 1 unit).

At 45ºC, it can be observed that having the inlet pressure at 1 bar or at 20 bar, the best porosity is always *eps* = 0.79756, and the best "n_i" is 7; however, in this last case Figure 3.34, the value of the current density for n_i = 8 is very close to the same value for n_i = 7.

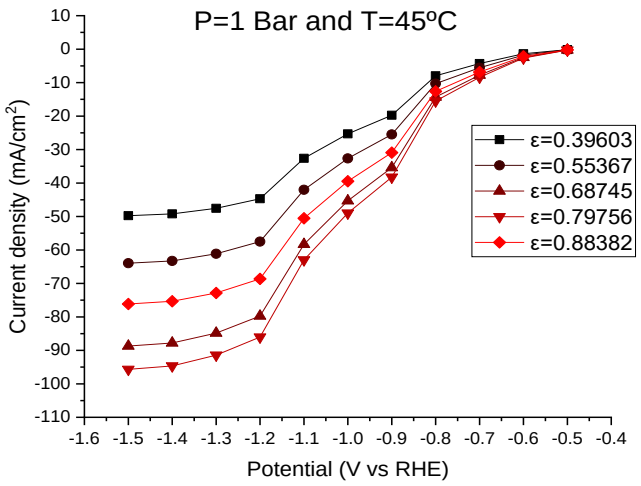

Figure 3.31: Polarization curves of different porosities at 1 bar and 45ºC.

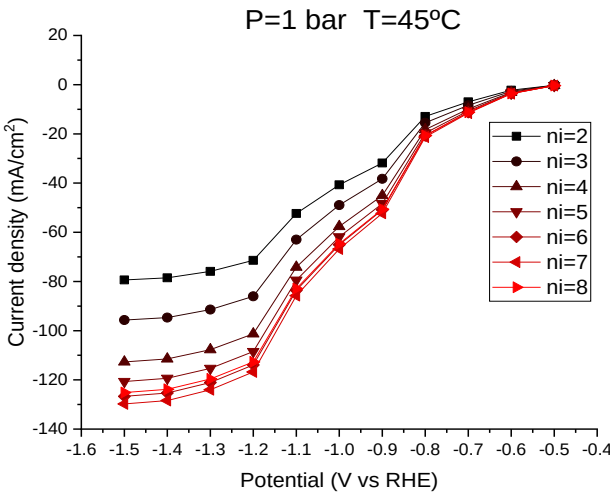

Figure 3.32: Polarization curves for the different "n_i's", with porosity 0.79756 at 1 bar and 45ºC.

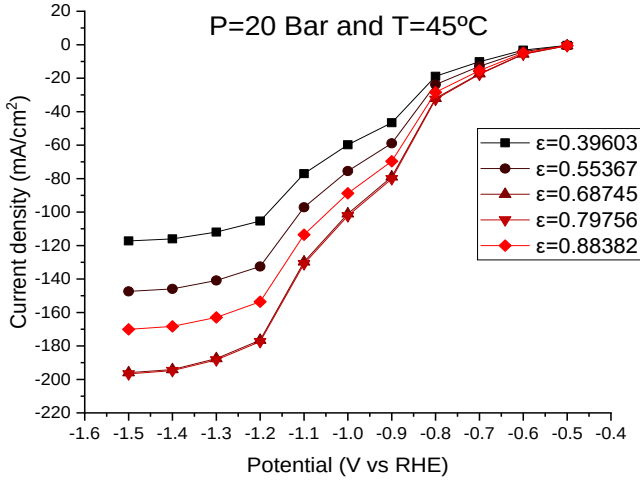

Figure 3.33: Polarization curves of different porosities at 20 bar and 45ºC.

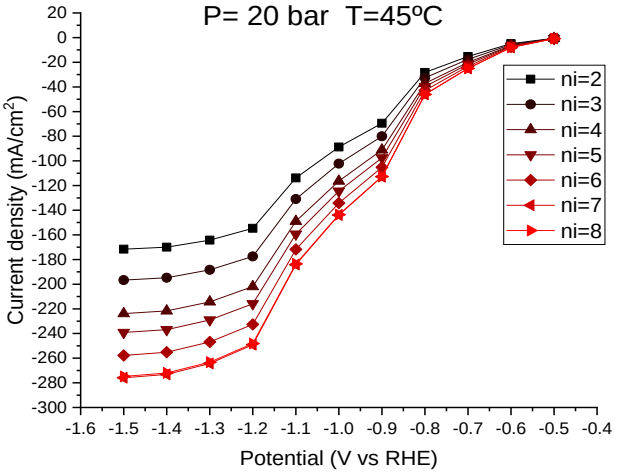

Figure 3.34: Polarization curves for the different "n_i's", with porosity 0.79756 at 20 bar and 45ºC.

In the case of increasing the temperature to 70ºC, the results are like those seen previously for 45ºC, with the best porosity for both cases (1 bar and 20 bar) being *eps* = 0.79756, and the best "n_i" being 7, resembling the situation seen previously for 45°C, where n_i = 7 and n_i = 8 have nearly identical behavior and differ little in terms of the current density value.

Looking at the current density findings in the study of the Polarization Curves for both the porosity and the "n_i" in general, one can observe that at 20 bar, whether it corresponds to 45ºC or to 70ºC, there is a significant increase in the current density. With the "n_i" optimization for these temperatures, with the inlet pressure of 20 bar, the current density is of approximately 280 mA/cm^2 (in absolute value), whereas with the inlet pressure of 1 bar is around 130 mA/cm^2, at most (both at 45ºC and 70ºC).

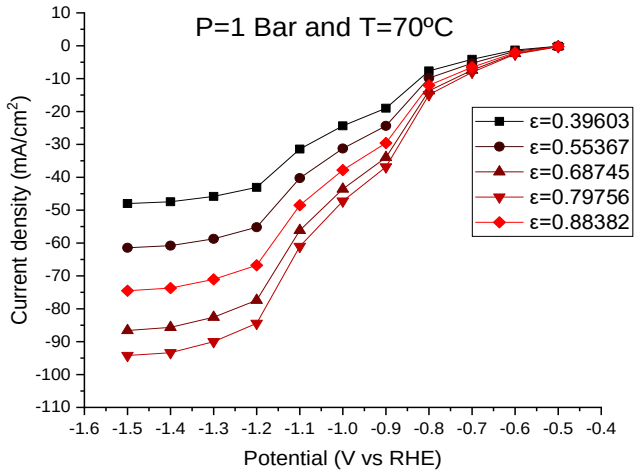

Figure 3.35: Polarization curves of different porosities at 1 bar and 70ºC.

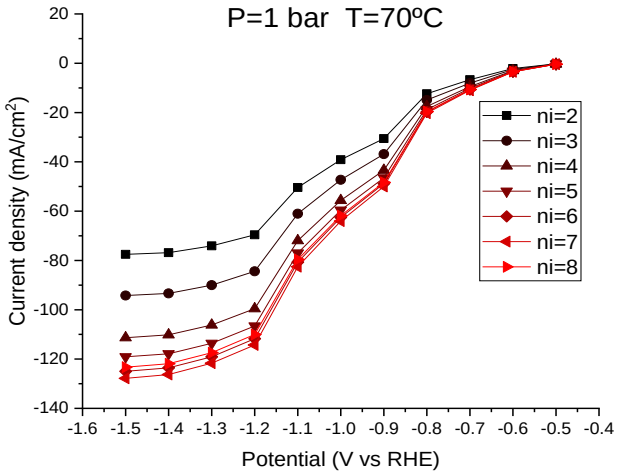

Figure 3.36: Polarization curves for the different "n_i's", with porosity 0.79756 at 1 bar and 70ºC.

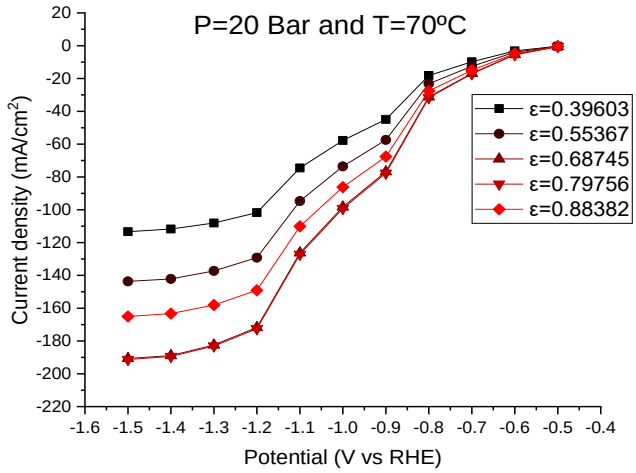

Figure 3.37: Polarization curves of different porosities at 20 bar and 70ºC.

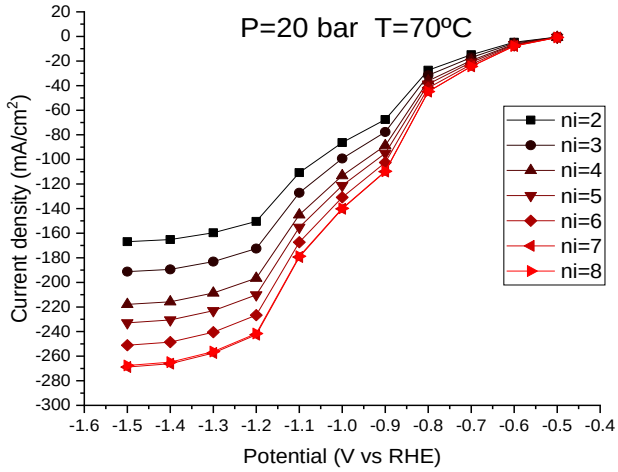

Figure 3.38: Polarization curves for the different "n_i's", with porosity 0.79756 at 20 bar and 70ºC.

In the Contour Plots investigation, we set the applied potential to -1.10 V vs. RHE, considering a porosity's range of 0.3 to 0.9, and a number of pores on the cathode side's range of 2 to 8.

According to the study of the Polarization Curves, there was a uniformity of results, which is also confirmed by the four Contour Plots shown below. The red "spot", i.e., where there is higher current density, is in the same place in all the figures, under all the conditions studied.

This zone is characterized by porosity values ranging from 0.7 to 0.8 and "n_i" values ranging from 7 to 8. When the pressure climbs from 1 bar to 20 bar, the value of the current density increases significantly (something which had already been noticed in the previous study and which is now corroborated). However, the change in the current density values when temperature is varied is not considerable, thus the energy expenditure of this process is not justified, given that at 45°C it reaches around 188.5 mA/cm^2, and at 70°C it reaches about 190.5 mA/cm^2 (in absolute values of current density).

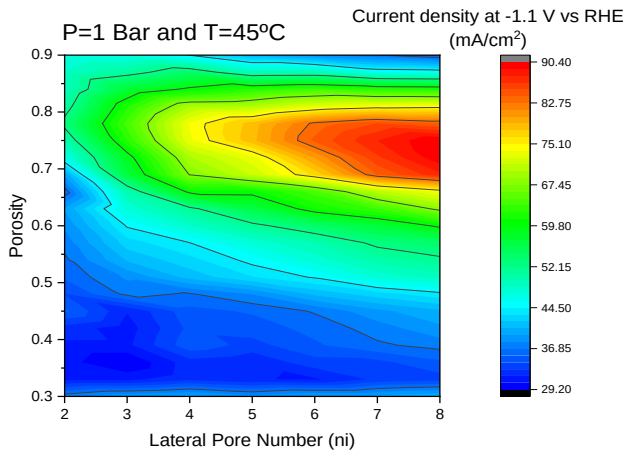

Figure 3.39: Circular shape fiber's Contour Plot of the porous zinc cathode at 1 bar and 45ºC.

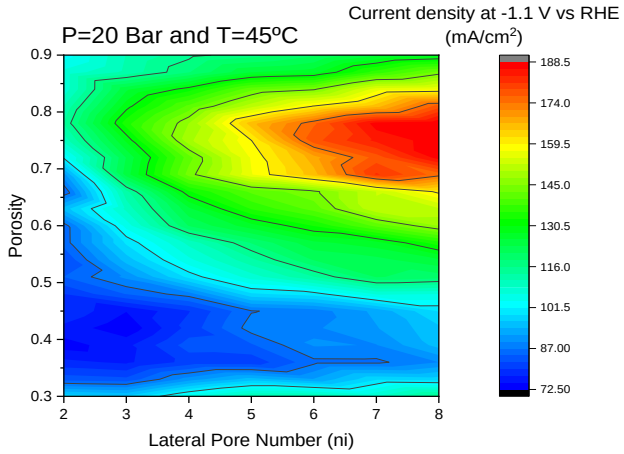

Figure 3.40: Circular shape fiber's Contour Plot of the porous zinc cathode at 20 bar and 45ºC.

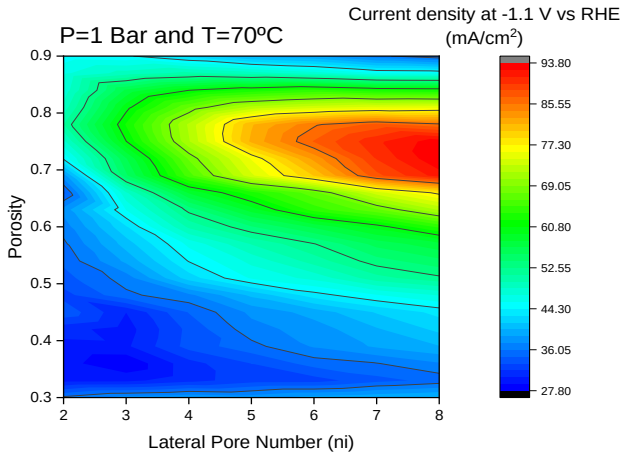

Figure 3.41: Circular shape fiber's Contour Plot of the porous zinc cathode at 1 bar and 70ºC.

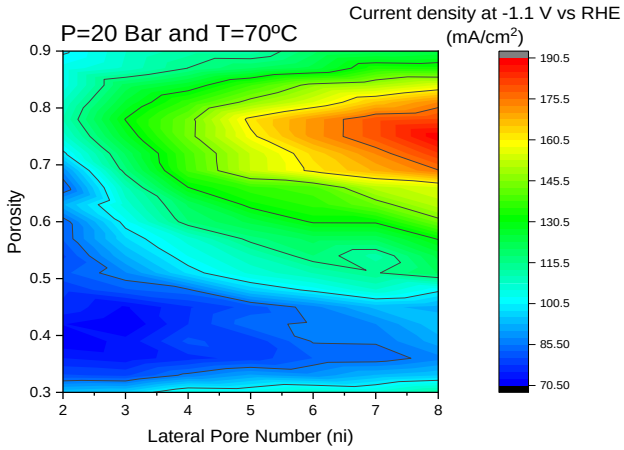

Figure 3.42: Circular shape fiber's Contour Plot of the porous zinc cathode at 20 bar and 70ºC.

4 Conclusions and Future Perspectives

A two-dimensional computational model for porous electrodes was successfully created, validated and corroborated in this Master's Thesis, allowing the design and optimization of a porous zinc cathode for an electrolizer to perform the co-electrolysis of CO_2 and water.

The effect of the cathode's morphological features, such as porosity, pore length and fiber shape geometry, as well as pressure and temperature parameters, might be studied using this model. This analysis will serve as a guide for and an aid in the experimental production of porous electrodes.

After all the simulations have been completed, it is feasible to draw extremely specific conclusions regarding the model's optimization.

As seen in Figure 4.1, the current density increased as the model was developed, and certain modifications were made. In comparison to Luo *et al.* (2019), which was the experimental reference article of this work, an increase of roughly 48% was obtained, which can be seen on the second bar (orange), representative of the first optimization process made.

Following that, more research was conducted on the alteration of the geometry of the model, and it was discovered that there was possible an increase of nearly 100% in comparison to the first optimization procedure.

A pressure and temperature variation investigation was conducted, where was achieved a considerable increase in the current density, close to 320%, comparing with the reference article, when temperature and pressure were increased. However, this does not justify the energy expenditure from 45°C to 70°C. Changing only the inlet pressure resulted in an increase compared to our initial investigation, although notably smaller than that of the cathode's geometries study. Again, the energy expense to boost that pressure from 5 to 10 bar is not justified by the enhancement obtained in the system performance.

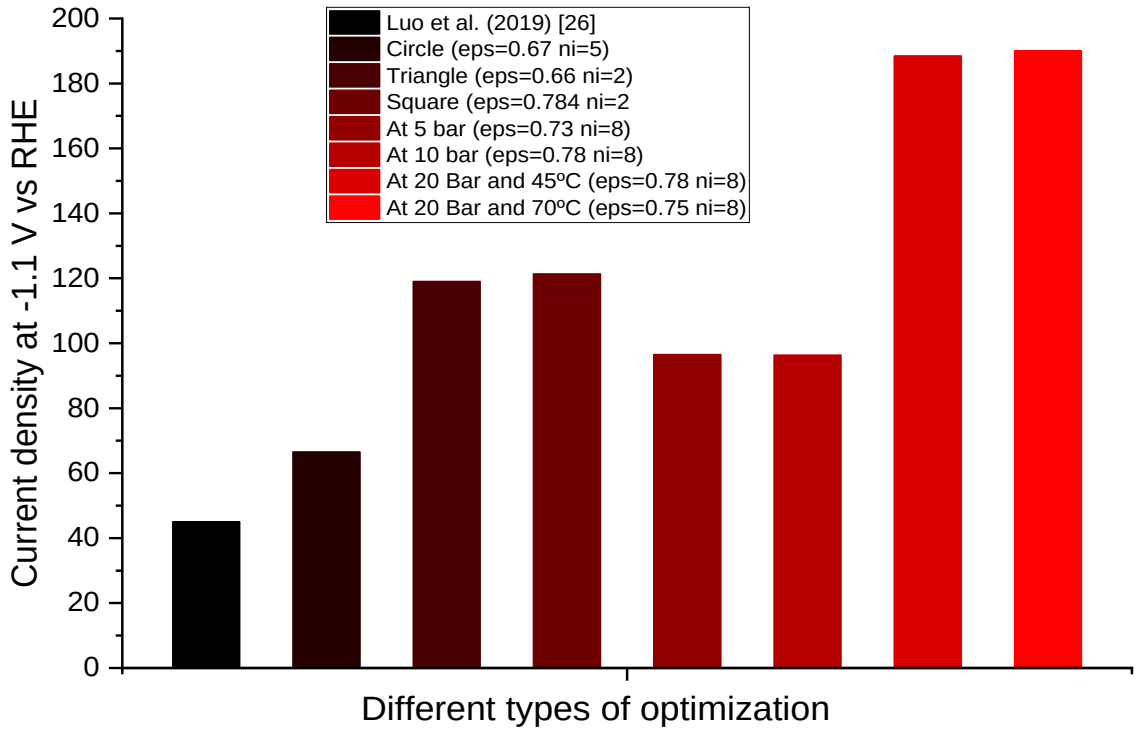

Figure 4.1: The different types of optimizations of the porous zinc cathode's model.

4.1 Future Perspectives

As time goes by, CO_2 emissions must be reduced, and if they do not, alternatives must be used. The CO_2 electroreduction is one of these options, and it is theoretically conceivable.

After finishing this work, I believe it is important to implement the various geometric designs that considerably improved the current density under the optimal operational conditions I achieved (20 bar and 45°C). The current density result will almost certainly be higher than what has already been achieved with this work.

The porous zinc cathode's 2D geometries modeled in this work have few solid electrode fibers and their total plain electrode surface areas are in the one mm^2 range. However, the results achieved in this work do not prevent the extension of these simulations behaviour to all areas of a larger porous electrode with the same geometric characteristics and subjected to similar operational conditions.

3D printing technology is already a reality, with a low cost and plenty of versatility, and it can make electrodes on a commercial scale for a reasonable price. It is a potential possibility for the construction of porous electrodes that are exactly fitted to the simplified geometric specifications of the simulated models. [34]

This will enable the creation of porous electrode modeling techniques with improved experimental validation reliability, using computer software such as the one utilized in this Master's Thesis, COMSOL Multiphysics®.

Furthermore, after all these optimizations done in this Thesis' Models, to do a more in-depth analysis of the modeling processes, and other possible experimental, or theoretical, validations/corroborations, will always be important to solidify the possible future use of the created models in real life scenarios.

The investigation of the behavior of the simulated porous zinc cathodes in 3D dimensions models using the COMSOL Multiphysics® software, and their incorporation in an electrolyzer model with the same electrochemical reaction (CO_2 reduction) and the water co-electrolysis, will also be a major improvement in the continuation of this project, in terms of approaching the modeling of a electrolyzer prototype device, which can be latter experimentally validated, or even actually built in laboratory scale (perhaps even industrially produced sometime in the future), to generate green syngas from CO_2 and water, powered by electricity derived from solar energy, creating a completely green process of producing renewable fuel capable of closing the carbon-dioxide exponential emissions cycle.

5 Bibliography

[1] "Page d'accueil GDR Solar Fuels - GDR Solar Fuels." https://solarfuels.cnrs.fr/ (accessed Oct. 12, 2022).

[2] F. Martins, C. Felgueiras, M. Smitkova, and N. Caetano, "Analysis of fossil fuel energy consumption and environmental impacts in european countries," *Energies*, vol. 12, no. 6, pp. 1–11, 2019, doi: 10.3390/en12060964.

[3] S. C. Bhattacharyya, 2019, "The Economics of Renewable Energy Supply," in *Energy Economics*. 2nd ed. Springer London, pp. 217–248, doi: 10.1007/978-1-4471-7468-4_8.

[4] M. B. Hayat, D. Ali, K. C. Monyake, L. Alagha, and N. Ahmed, "Solar energy - A look into power generation, challenges, and a solar-powered future," *Int. J. Energy Res.*, vol. 43, no. 3, pp. 1049–1067, 2019, doi: 10.1002/er.4252.

[5] R. J. Detz, J. N. H. Reek, and B. C. C. Van Der Zwaan, "The future of solar fuels: When could they become competitive?," *Energy Environ. Sci.*, vol. 11, no. 7, pp. 1653–1669, 2018, doi: 10.1039/c8ee00111a.

[6] D. Gust, T. A. Moore, and A. L. Moore, "Solar fuels via artificial photosynthesis," *Acc. Chem. Res.*, vol. 42, no. 12, pp. 1890–1898, 2009, doi: 10.1021/ar900209b.

[7] N. Roy, N. Suzuki, C. Terashima, and A. Fujishima, "Recent improvements in the production of solar fuels: From CO2 reduction to water splitting and artificial photosynthesis," *Bull. Chem. Soc. Jpn.*, vol. 92, no. 1, pp. 178–192, 2019, doi: 10.1246/bcsj.20180250.

[8] D. K. Dogutan and D. G. Nocera, "Artificial Photosynthesis at Efficiencies Greatly Exceeding That of Natural Photosynthesis," *Acc. Chem. Res.*, vol. 17, pp. 3143–3148, 2019, doi:10.1021/ACS.ACCOUNTS.9B00380.

[9] I. McConnell, G. Li, and G. W. Brudvig, "Energy conversion in natural and artificial photosynthesis," *Chem. Biol.*, vol. 17, no. 5, pp. 434–447, 2010, doi: 10.1016/j.chembiol.2010.05.005.

[10] "Natural photosynthesis vs. artificial photosynthesis. Download Scientific Diagram." https://www.researchgate.net/figure/Natural-photosynthesis-vs-artificial-photosynthesis_fig2_326356800 (accessed Oct. 07, 2022).

[11] R. J. Detz, J. N. H. Reek, and B. C. C. Van Der Zwaan, "The future of solar fuels: When could they become competitive?," *Energy Environ. Sci.*, vol. 11, no. 7, pp. 1653–1669, 2018, doi: 10.1039/c8ee00111a.

[12] E. Zoulias and E. Varkaraki, "A review on water electrolysis," *Tcjst*, vol. 4, no. 2, pp. 41–71, 2004, [Online]. Available: http://large.stanford.edu/courses/2012/ph240/jorna1/docs/zoulias.pdf.

[13] H. Nazir, C. Louis, S. Jose, J. Prakash, N. Muthuswamy, M. E. M. Buan, C. Flox, S. Chavan, X. Shi, P. Kauranen, T. Kallio, G. Maia, K. Tammeveski, N. Lymperopoulos, E. Carcadea, E. Veziroglu, A. Iranzo, A. M. Kannan, "Is the H2 economy realizable in the foreseeable future? Part I: H2 production methods," *Int. J. Hydrogen Energy*, vol. 45, no. 27, pp. 13777–13788, 2020, doi: 10.1016/j.ijhydene.2020.03.092.

[14] "Hydrogen Production: Electrolysis, Department of Energy." https://www.energy.gov/eere/fuelcells/hydrogen-production-electrolysis (accessed Oct. 07, 2022).

[15] H. Schulz, "Short history and present trends of Fischer-Tropsch synthesis," *Appl. Catal. A Gen.*, vol. 186, no. 1–2, pp. 3–12, 1999, doi: 10.1016/S0926-860X(99)00160-X.

[16] IOGP, "The potential for CCS and CCU in Europe," *Rep. to thirty Second Meet. Eur. Gas Regul. Forum 5-6 June 2019.*, no. June, pp. 1–47, 2019.

[17] S. Garg, M. Li, A. Z. Weber, L. Ge, L. Li, V. Rudolph, G. Wang, T. E. Rufford, "Advances and challenges in electrochemical CO2 reduction processes: An engineering and design perspective looking beyond new catalyst materials," *J. Mater. Chem. A*, vol. 8, no. 4, pp. 1511–1544, 2020, doi: 10.1039/c9ta13298h.

[18] A. Alok, R. Shrestha, S. Ban, S. Devkota, B. Uprety, and R. Joshi, "Technological advances in the transformative utilization of CO2 to value-added products," *J. Environ. Chem. Eng.*, vol. 10, no. 1, p. 106922, Feb. 2022, doi: 10.1016/J.JECE.2021.106922.

[19] L. Zhang, Z. J. Zhao, and J. Gong, "Nanostructured Materials for Heterogeneous Electrocatalytic CO2 Reduction and their Related Reaction Mechanisms," *Angew. Chemie - Int. Ed.*, vol. 56, no. 38, pp. 11326–11353, 2017, doi: 10.1002/anie.201612214.

[20] "Electrolyzers 101: What they are, how they work and where they fit in a green economy | Cummins

Inc." https://www.cummins.com/news/2020/11/16/electrolyzers-101-what-they-are-how-they-work-and-where-they-fit-green-economy (accessed Oct. 07, 2022).
[21] C. Ma, X. Li, L. Lin, L. Chen, M. Wang, and J. Zhou, "A two-dimensional porous electrode model for designing pore structure in a quinone-based flow cell," *J. Energy Storage*, vol. 18, no. April, pp. 16–25, 2018, doi: 10.1016/j.est.2018.04.007.
[22] "COMSOL - Software for Multiphysics Simulation." https://www.comsol.com/ (accessed Oct. 07, 2022).
[23] "Which Current Distribution Interface Do I Use? COMSOL Blog." https://www.comsol.com/blogs/current-distribution-interface-use/ (accessed Oct. 07, 2022).
[24] "The Creeping Flow Interface." https://doc.comsol.com/6.0/doc/com.comsol.help.cfd/cfd_ug_fluidflow_single.06.007.html (accessed Oct. 07, 2022).
[25] "The Transport of Diluted Species Interface." https://doc.comsol.com/5.6/doc/com.comsol.help.chem/chem_ug_chemsptrans.08.049.html (accessed Oct. 07, 2022).
[26] W. Luo, J. Zhang, M. Li, and A. Züttel, "Boosting CO Production in Electrocatalytic CO2 Reduction on Highly Porous Zn Catalysts," *ACS Catal.*, vol. 9, no. 5, pp. 3783–3791, 2019, doi: 10.1021/acscatal.8b05109.
[27] A. Desalvo, P. Gondi, F. A. Levi, and F. Zignani, "Electrical conductivity of high-purity zinc," *Nuovo Cim*, vol. 31, no. 4, pp. 904–913, 1964, doi: 10.1007/BF02733804.
[28] R. O. Crowder and E. L. Cussler, "Mass transfer in hollow-fiber modules with non-uniform hollow fibers," *J. Memb. Sci.*, vol. 134, no. 2, pp. 235–244, 1997, doi: 10.1016/S0376-7388(97)00112-9.
[29] M. L. Pegis, J. A. S. Roberts, D. J. Wasylenko, E. A. Mader, A. M. Appel, and J. M. Mayer, "Standard Reduction Potentials for Oxygen and Carbon Dioxide Couples in Acetonitrile and N,N-Dimethylformamide," *Inorg. Chem.*, vol. 54, no. 24, pp. 11883–11888, 2015, doi: 10.1021/acs.inorgchem.5b02136.
[30] R. Chang and K. A. Goldsby, 2014. *Chemistry*. 11th ed. New York: McGraw-Hill Education.
[31] I. S. Fernandes, 2021. *Modelação de Cátodos Porosos para Redução Eletroquímica do CO2: Uma Abordagem de Modelação em COMSOL Multiphysics*®. Thesis.
[32] E. L. Cussler, 1997. *Diffusion: Mass transfer in Fluid Systems.* 2nd ed. Cambridge University Press.
[33] G. Bisweswar, A. Al-Hamairi, and S. Jin, "Carbonated water injection: an efficient EOR approach. A review of fundamentals and prospects," *J. Pet. Explor. Prod. Technol.*, vol. 10, no. 2, pp. 673–685, 2020, doi: 10.1007/s13202-019-0738-2.
[34] A. da Silveira, J. Bonacin, N. Gasbarro, T. Ferraz, and P. dos Santos, 2019, in *Desenvolvimento de elétrodos impressos em 3D modificados com Ni(OH)2 para estudos de oxidação de água*. Campinas, SP: Revista dos Trabalhos de Iniciação Científica da UNICAMP, doi: 10.20396/revpibic2720192475.

A. Annex

A.1 Thesis Model Corroboration

A.1.1 Thesis Model's Results using Butler-Volmer Equation

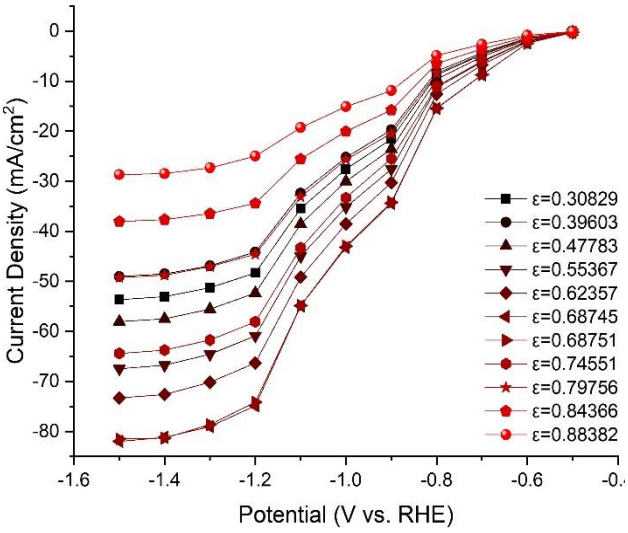

Figure A.1: Polarization curves for different porosities.

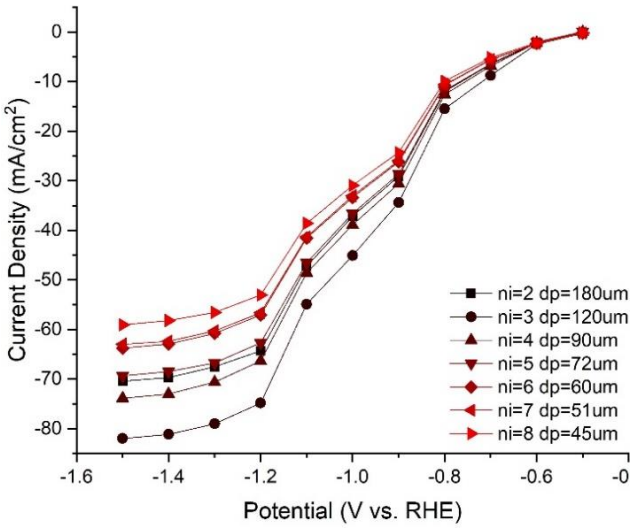

Figure A.2: Polarization curves for the different "n_i's" with porosity 0.68745.

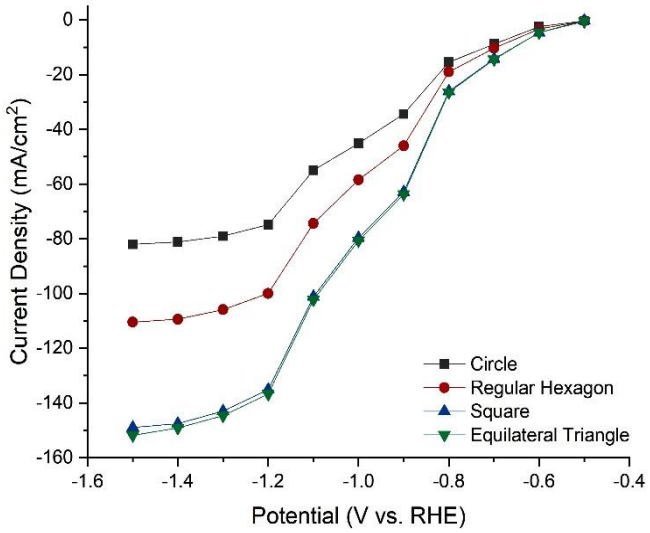

Figure A.3: Polarization curves of different geometric fiber shapes with a lateral pore number of 3.

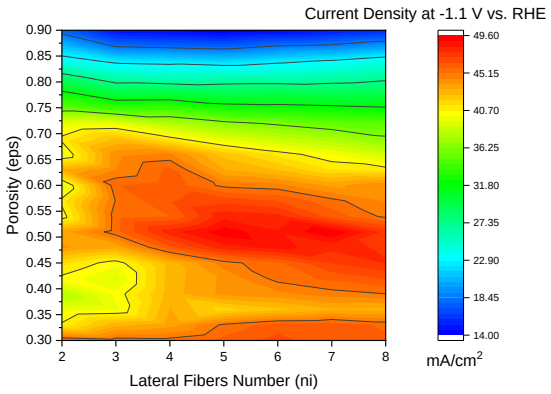

Figure A.4: Circular shape fiber's Contour Plot of the porous zinc cathode.

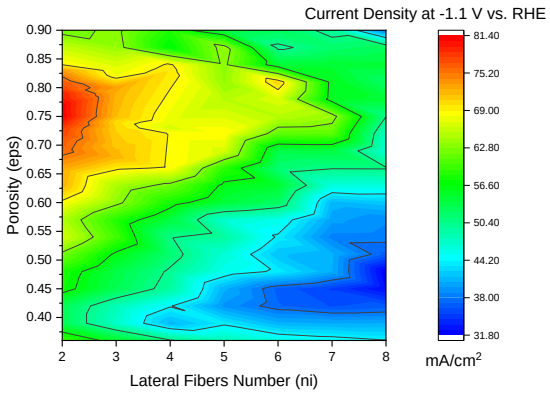

Figure A.5: Regular hexagonal shape fiber's Contour Plot of the porous zinc cathode.

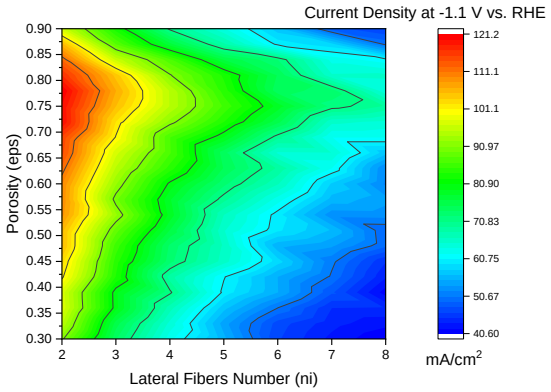

Figure A.6: Square shape fiber's Contour Plot of the porous zinc cathode.

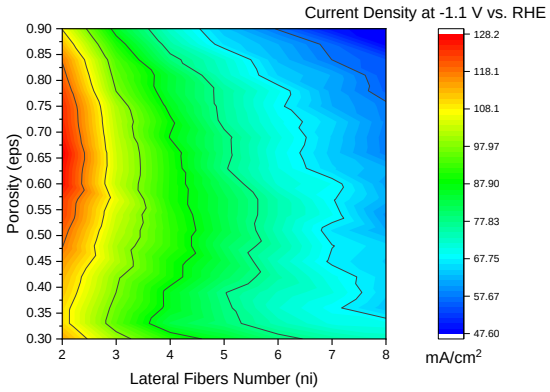

Figure A.7: Equilateral triangular shape fiber's Contour Plot of the porous zinc cathode.

A.1.2 Ma *et al.* (2018) Replicated Model's Results (Adapted from the Thesis Model)

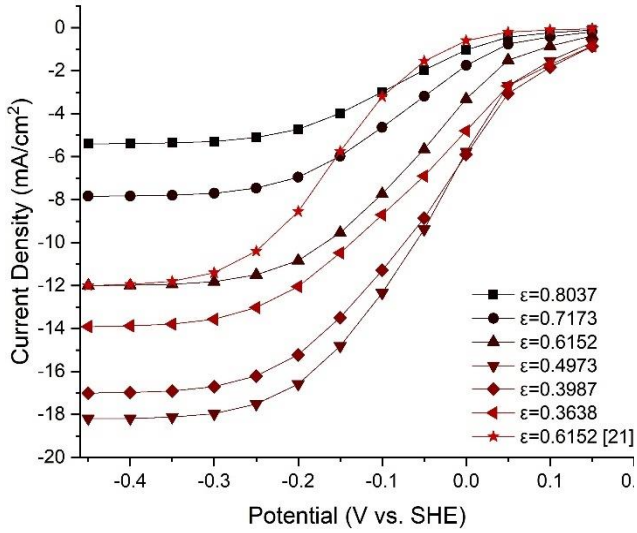

Figure A.8: Polarization curves for different porosities. [21]

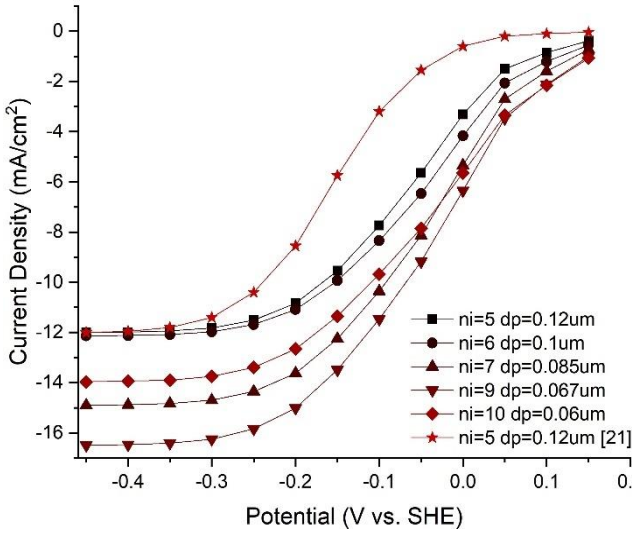

Figure A.9: Polarization curves for the different "n_i's" with porosity 0.6152. [21]

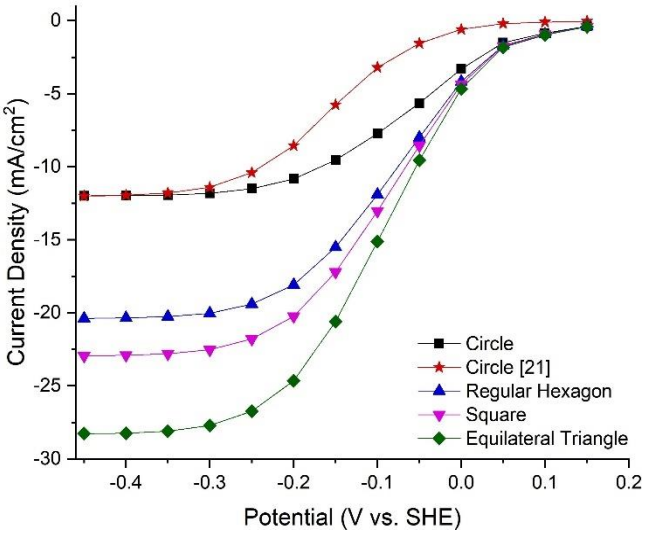

Figure A.10: Polarization curves of different geometric fiber shapes with a lateral pore number of 5. [21]

2022

DUARTE CORREIA DA FONSECA
DA SILVA ANTUNES

SOLAR FUELS DESIGN: MODELING POROUS CATHODES FOR THE PRODUCTION OF CARBON-BASED FUELS FROM CO_2

NOVA SCHOOL OF
SCIENCE & TECHNOLOGY